

Quantum control of continuous systems via nonharmonic potential modulation

Piotr T. Grochowski^{1,2,3}, Hannes Pichler^{1,2}, Cindy A. Regal^{4,5}, and Oriol Romero-Isart^{1,2,6,7}

¹Institute for Quantum Optics and Quantum Information of the Austrian Academy of Sciences, A-6020 Innsbruck, Austria

²Institute for Theoretical Physics, University of Innsbruck, A-6020 Innsbruck, Austria

³Department of Optics, Palacký University, 17. listopadu 1192/12, 771 46 Olomouc, Czech Republic

⁴JILA, National Institute of Standards and Technology and University of Colorado, Boulder, Colorado 80309, USA

⁵Department of Physics, University of Colorado, Boulder, Colorado 80309, USA

⁶ICFO - Institut de Ciències Fòniques, The Barcelona Institute of Science and Technology, 08860 Castelldefels (Barcelona), Spain

⁷ICREA, Passeig Lluís Companys 23, 08010 Barcelona, Spain

We present a theoretical proposal for preparing and manipulating a state of a single continuous-variable degree of freedom confined to a nonharmonic potential. By utilizing optimally controlled modulation of the potential's position and depth, we demonstrate the generation of non-Gaussian states, including Fock, Gottesman-Kitaev-Preskill, multi-legged-cat, and cubic-phase states, as well as the implementation of arbitrary unitaries within a selected two-level subspace. Additionally, we propose protocols for single-shot orthogonal state discrimination, algorithmic cooling, and correcting for nonlinear evolution. We analyze the robustness of this control scheme against noise. Since all the presented protocols rely solely on the precise modulation of the effective nonharmonic potential landscape, they are relevant to several experiments with continuous-variable systems, including the motion of a single particle in an optical tweezer or lattice, or current in circuit quantum electrodynamics.

1 Introduction

The preparation of a continuous-variable system in a non-Gaussian quantum state is of paramount importance in various aspects of quantum science. This ranges from fundamental tests of quantum mechanics [1–5], through the design of quantum sensors [6–9], to quantum information processing [10–18]. The generation of non-Gaussian states requires a nonlinear resource, often introduced through coupling to an auxiliary degree of freedom, e.g., a two-level system [5, 12, 15, 19–22]. On the other hand, some continuous-variable systems already possess intrinsic nonharmonicity in the potential of a canonical variable. Notable examples include the motion of a par-

Piotr T. Grochowski: piotr.grochowski@upol.cz

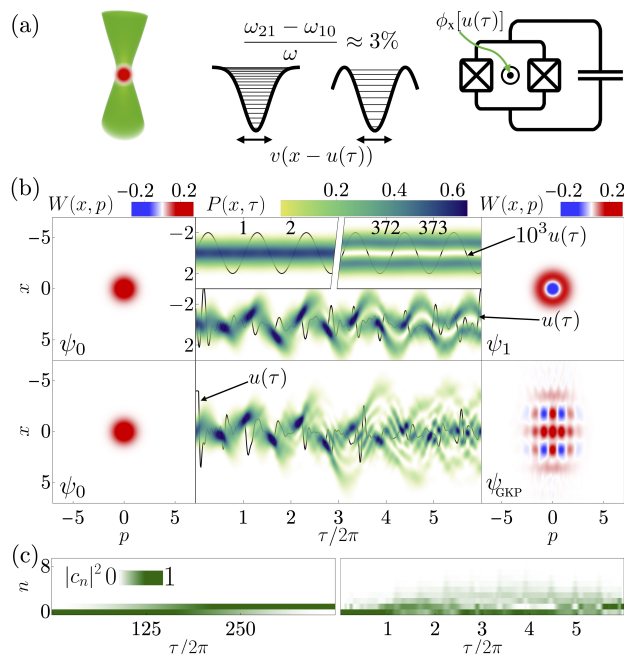


Figure 1: (a) Examples of continuous-variable nonlinear systems that can be optimally controlled without the need of auxiliary systems—single atoms in optical tweezers and flux-tunable transmons. (b) Time-evolved probability density $P(x, \tau) = |\psi(x, \tau)|^2$, during the state preparation protocol with the snapshots of Wigner functions $W(x, p)$ at the beginning and the end of the protocol. The potential is Gaussian and its optimally controlled position $u(\tau)$ is depicted via a solid black line. The top panel shows a comparison between a weak and long sinusoidal drive resonant with the ground-first excited state transition and an optimized much faster control. The bottom panel presents an optimal control leading to the GKP state. (c) Excited states occupation numbers $|c_n(\tau)|^2 = |\langle \psi_n(x) | \psi(x, \tau) \rangle|^2$ for $\psi_0(x) \rightarrow \psi_1(x)$ Fock excitation protocols of (b)top. The left panel corresponds to the slow Rabi flop, while the right one shows the fast optimal control. Utilizing more states within the nonharmonic potential accelerates and makes the control more versatile.

title in a trap of finite depth [23, 24] and the current in an electric circuit with a Josephson junction [25]. These nonharmonicities in the potential are typically

used to define a qubit within continuous-variable systems [26–30]. In contrast, we explore methods for utilizing this intrinsic nonlinearity to generate and control states beyond the two-dimensional subspace.

More specifically, we develop protocols to generate a plethora of states, including Fock, Gottesman-Kitaev-Preskill (GKP) [10], multi-legged-cat [1, 31], and cubic-phase [10, 32], using optimal control [33–35] of the potential’s position and depth. Furthermore, we employ this control mechanism to design protocols that implement arbitrary unitaries in selected subspaces, enable single-shot orthogonal state discrimination [36, 37], spatial state transfer, correct for nonlinear evolution, and perform algorithmic cooling [38, 39]. These protocols could be implemented with single atoms in optical tweezers [40–44] and lattices [23, 45] to extend the motional states available in protocols with itinerant particles, e.g., fermionic quantum processors [18]; or with flux-tunable transmons [25, 28, 46] for minimally invasive state manipulation [cf. Fig 1(a)]. Previous works, including control of Bose-Einstein condensates [47–56], fast atom transport [45, 57, 58], ion shuttling [59], cat state creation through two-photon driving [60], and lattice interferometry [61] have demonstrated similar concepts. However, the impact of nonharmonic potentials in quantum information processing has yet to be fully realized, despite being a natural area of exploration—especially given the potential to utilize, for example, the motion of single atoms in scalable optical tweezer arrays [39].

The preparation of continuous-variable modes in quantum non-Gaussian states and their subsequent manipulation have been an object of increasing interest across several platforms, including single neutral atoms [44], trapped ions [62–65], superconducting circuits [66–68], propagating light at the telecommunication wavelength [69, 70], etc. The control scheme we present offers a realization of a large variety of relevant tasks and can be applied to a generic continuous-variable platform that involves nonharmonicity. Our protocols take advantage of the controllability of the external potential landscape, naturally offered by, e.g., optical [39, 44, 45], electric [24], and magnetic [71–73] potentials, and their hybrid combinations [62–65, 74]. With such schemes, a high information capacity of bosonic degree of freedom is activated via preparation and control of high-energy and high-quality quantum non-Gaussian states. Our protocols are particularly interesting and useful for systems without well-controlled access to nonlinear resources, e.g., internal degrees of freedom or auxiliary superconducting circuits. However, they can also be combined with such couplings for simultaneous control of both bosonic and spin degrees of freedom, opening new possibilities for, e.g., the use of hyperentanglement [75].

The paper is structured as follows. Section 2 in-

troduces details about the physical model and optimization techniques, while Section 3 presents several protocols that can be achieved through potential modulation, including state preparation, implementation of unitaries, single-shot measurements, cooling, correcting for nonlinear evolution, and spatial state transfer. Further, Section 4 analyzes the feasibility of our proposal, addressing the speed limits of the protocols, their robustness against decoherence, and how couplings to other modes can be incorporated into optimization. Section 5 concludes the paper with a finishing discussion and an outlook.

2 Control of potential landscape

In the following Section, we present two exemplary realizations of one-dimensional continuous-variable systems for which our proposal can be applied—a single neutral atom trapped via optical forces, either in a tweezer or in a lattice, and a flux-tunable transmon. In the Subsection 2.1, we provide details of the involved Hamiltonians in these platforms, introduce a universal description of our control scheme, and address how much nonharmonicity is needed for the presented protocols. The Subsection 2.2 is dedicated to details on the control optimization of our scheme.

2.1 Hamiltonians for different systems

As a starting point, we focus on a one-dimensional continuous-variable system described by two conjugate quadrature operators, which may correspond to an arbitrary realization of a single mode, e.g., the motion of a single atom in an optical tweezer [44, 76, 77] or a lattice [45, 78], or phase and charge operators in a flux-tunable transmon [25, 79, 80]. In the former case, coherent dynamics is driven by a Hamiltonian,

$$\hat{H} = \frac{\hat{P}^2}{2m} + [1 + a(t)] V [\hat{X} - U(t)], \quad (1)$$

where m is the mass of an atom, \hat{X} is the position operator, \hat{P} is the momentum operator, t is time, and functions $a(t)$ and $U(t)$ control the depth and position of the potential. Here, the trapping potential $V(\hat{X})$ is Gaussian for the tweezer,

$$V(\hat{X}) = V_0 \left(1 - e^{-\frac{2\hat{X}^2}{w_0^2}} \right), \quad (2)$$

and a squared sine for the lattice,

$$V(\hat{X}) = V_0 \sin^2 \left(\frac{2\pi}{\lambda} \hat{X} \right), \quad (3)$$

where w_0 is the tweezer waist, λ is the optical wavelength, and V_0 is either the tweezer or the lattice

depth. For the transmon case, the Hamiltonian reads

$$\hat{H} = 4E_C \hat{n}^2 + E_J \cos\left(\frac{\pi\phi_x(t)}{\Phi_0}\right) \sqrt{1 + d^2 \tan^2 \frac{\pi\phi_x(t)}{\Phi_0}} \times \left[1 - \cos\left(\hat{\varphi} - d \tan \frac{\pi\phi_x(t)}{\Phi_0}\right)\right]. \quad (4)$$

Here, $\hat{\varphi} = (\hat{\varphi}_1 + \hat{\varphi}_2)/2$ is the phase difference operator, $\hat{n} = \hat{Q}/2e$ is charge number operator, $\hat{\varphi}_i = 2\pi\hat{\Phi}_i/\Phi_0$ is phase difference across i^{th} junction, $\Phi_0 = h/2e$ is the flux quantum, $E_C/h = e^2/2hC$ is the charge energy, C is the total capacitance, $E_J = E_{J1} + E_{J2}$ is the total Josephson energy, E_{Ji} is the Josephson energy of i^{th} junction, $d = (E_{J2} - E_{J1})/(E_{J2} + E_{J1})$ is the junction asymmetry, and $\phi_x(t)$ is the external flux through SQUID.

In the leading order, each of these setups is harmonic with frequency ω , yielding natural time $\tau = \omega t$, canonical length and momentum scales,

$$\hat{x} = \frac{\hat{X}}{X_0} = \frac{\hat{n}}{n_0} = \frac{1}{\sqrt{2}}(\hat{a}^\dagger + \hat{a}),$$

$$\hat{p} = \frac{\hat{P}}{P_0} = \frac{\hat{\varphi}}{\varphi_0} = \frac{1}{\sqrt{2}}i(\hat{a}^\dagger - \hat{a}), \quad (5)$$

where \hat{a}^\dagger creates a single excitation. For an atom trapped in a tweezer, we have

$$X_0 = (\hbar^2 w_0^2 / 4mV_0)^{1/4},$$

$$P_0 = \hbar/X_0,$$

$$\omega = \sqrt{4V_0/mw_0^2}, \quad (6)$$

while for the optical lattice,

$$X_0 = (\hbar^2 \lambda^2 / 8\pi^2 mV_0)^{1/4},$$

$$P_0 = \hbar/X_0,$$

$$\omega = \sqrt{8\pi^2 V_0/m\lambda^2}. \quad (7)$$

For the flux-tunable transmon, the canonical length and momentum scales read

$$n_0 = (8E_C/E_J)^{1/4},$$

$$\varphi_0 = 1/n_0,$$

$$\omega = \sqrt{8E_C E_J}/\hbar. \quad (8)$$

In the canonical variables \hat{x} , \hat{p} , each of the Hamiltonians (1), (4) can be rewritten as

$$\frac{\hat{H}}{\hbar\omega} = \frac{1}{2}\hat{p}^2 + [1 + a(\tau)]v[\hat{x} - u(\tau)], \quad (9)$$

where $v = V/\hbar\omega$ is the dimensionless potential. The control of the system is performed through optimal modulation of position, $u(\tau)$, and depth, $a(\tau)$, of the potential. While for an atom in an optical tweezer, they are independent controls realized through, e.g.,

acousto-optic modulator [77], for flux-tunable transmons they are constrained through a single control function, the intensity of the external flux [79],

$$a(\tau) = \sqrt{\frac{1 + 4\sqrt{E_C/2E_J}u^2(\tau)}{1 + 4\sqrt{E_C/2E_J}u^2(\tau)d^{-2}}} - 1,$$

$$u(\tau) = \frac{d}{2\eta} \tan \frac{\pi\phi_x(\tau)}{\Phi_0}. \quad (10)$$

Such modulations have been realized in various other experimental platforms [45, 54, 55, 61, 81], where the choice of either position or depth control depends on feasibility within a specific setup. For example, Paul traps allow for both position and depth control via varying current through electrodes generating the electric field [54], while in optical lattices phase control allows very precise position control [45]. As for optical tweezers, the use of multiple radiofrequency tones makes a powerful knob for the time-dependent control of both position and depth [44].

In general, we consider the shape of the potential to be symmetric in x , and we find it useful to express it as

$$v(x) = \frac{1}{2\eta^2}v_0(\eta x) \approx \frac{1}{2}x^2 - \frac{1}{6}\eta^2 x^4 \quad (11)$$

when expanded up to the second order in the small parameter η . For the examples considered in this work, the tweezer potential then reads as

$$v_0(x) = \frac{3}{2} \left[1 - \exp\left(-\frac{2}{3}x^2\right)\right], \quad (12)$$

while for the lattice it is

$$v_0(x) = \sin^2 x, \quad (13)$$

and for the flux-tunable transmon,

$$v_0(x) = \frac{1}{2}[1 - \cos(2x)] \quad (14)$$

Note we have defined the units so that the functional forms of these potentials match up to the second leading order, allowing for a unified discussion of nonharmonicity. Here, η is the measure of the nonharmonicity of the potential, comparing the canonical length to the characteristic length scale of the potential, and translates directly into an energy level splitting,

$$\frac{\omega_{21} - \omega_{10}}{\omega} = -\frac{1}{2}\eta^2, \quad (15)$$

where ω_{ij} is a transition frequency between i^{th} and j^{th} levels. For instance, for an atom in a tweezer it is

$$\eta = \sqrt{3}\frac{X_0}{w_0}; \quad (16)$$

for an optical lattice, it is a Lamb-Dicke parameter

$$\eta = \frac{2\pi X_0}{\lambda}; \quad (17)$$

for the flux-tunable transmon it is a monotonic function of transmon anharmonicity α ,

$$\frac{\alpha}{\omega} = \sqrt{\frac{E_C}{8E_J}} = \frac{1}{2}\eta^2, \quad (18)$$

and for Kerr oscillators, it can be associated with Kerr nonlinearity $\kappa \sim \omega\eta^2/24$ [82]. The typical values of physical parameters for the examples introduced in this section lead to nonharmonicities no larger than $\eta \sim 0.5$ (see Tab. 1) and can be tuned down at least an order of magnitude depending on the specific setup. Hence, here we will analyze such a parameter regime. Nevertheless, many other experimental platforms are characterized by much lower values, such as trapped ions [24, 83] or levitated mechanical oscillators [84, 85]. There, lower nonharmonicity is associated with either larger potential length scales or larger masses of trapped objects. In such cases, the additional enhancement of nonharmonicity is needed, e.g., through state excitation [85–87], to generate non-Gaussian states.

Optically trapped atom		Superconducting circuit	
m	10^1 - 10^2 u	E_C/h	MHz-GHz
w_0, λ	10^2 - 10^3 nm	E_J	10^1 - $10^4 E_C$
V_0/k_B	μ K-mK	d	0-1

Table 1: Typical physical parameters for atoms held in optical tweezers or optical lattices and flux-tunable transmons.

2.2 Control optimization

Before presenting specific protocols, let us discuss possible methods of designing controls $u(\tau)$ and $a(\tau)$. Within each of the subsequent protocols, we aim to achieve some specific goal—be it state preparation, unitary implementation, or others—that can be quantified through a reward function that ought to be maximized. A set of methods for designing time-varying controls for the maximization of such a reward function is collectively called *quantum optimal control* (QOC) [33, 34, 88]. Introduced in the eighties and since then broadly developed, QOC has become one of the main quantum control tools, among other optimization approaches, such as adiabatic passages [89], shortcuts to adiabaticity [90], and composite pulses [91]. Various techniques have been established to design the control pulses, relying on both gradient-free and gradient-based approaches. The latter assume the ability to differentiate the reward function and include, among the others, GRAPE (gradient ascent pulse engineering)- [92] and Krotov-like [93, 94] techniques for optimizing controls that are piecewise constant in time. On the other hand, the former rely only on the evaluation of the reward function itself. The examples are numerous, including Nelder-Mead [95], evolution strategies [96], simulated annealing [97], and many others. Notably, recent years

have brought a rapid surge in using machine learning approaches for quantum control problems [98]. The choice of approach relies on constraints given by a specific experimental setup, including how accurately and fast we can solve the dynamics and what the limitations of control pulses are, such as maximal Fourier bandwidth and intensity. We choose to utilize the dressed chopped random-basis technique (dCRAB) [99] that is based on the Nelder-Mead gradient-free method. Here, the control function is expanded into a Fourier basis with randomized frequencies and a high-frequency cutoff corresponding to approximations of experimentally accessible bandwidths, i.e.,

$$u(\tau) = \sum_{k=1}^{N_p} a_k \cos \nu_k \tau + b_k \sin \nu_k \tau, \quad (19)$$

where a_k and b_k are parameters to be optimized, ν_k are frequencies that are probabilistically drawn from the uniform distribution in the range $[0, \nu_{\max}]$, ν_{\max} is the frequency cutoff, and N_p is the number of frequency components. We have chosen this particular gradient-free method as we consider several different reward functions, it naturally implements a frequency cutoff for the control function, and there are available well-developed open-source packages, including the Quantum Optimal Control Suite [35] which we utilize for the optimization. However, depending on the specifics of the experimental implementation, our results can be achieved with an alternative approach, such as, e.g., GRAPE.

For all the simulations, the split-step method [100] was used to simulate the dynamics on a spatial grid. In the case of one-dimensional calculations, throughout optimization runs, the numerical parameters read: number of spatial grid points $N_x = 2^8$, where the grid spanned $x \in [-13, 13]$, and number of time grid points $N_\tau = 500$. After optimizing the pulses, the dynamics was run and further optimized with increased accuracy to make sure the results are converged. The optimization has been performed with QuoCS library version 0.0.44 [35]. The number of Fourier components used for dCRAB varied from 20 to 50 depending on a particular protocol and were randomized from a uniform distribution on a bandwidth that also varied between different protocols. The choice of these optimization parameters was fine-tuned for each of the protocols, however, it was not exclusive—different choices usually yielded similar values of specific reward functions, but with different total optimization iterations. Note that further optimization of all the protocols towards lower infidelities is possible and would involve further fine-tuning of optimization parameters.

3 Protocols

In the following section, we discuss several protocols that can be implemented via a nonharmonic potential modulation. It includes a versatile non-Gaussian state preparation, both in a single- (sec. 3.1) and double-well (sec. 3.3) potential landscape, as well as the implementation of unitaries (sec. 3.2), single-shot measurements (sec. 3.4), cooling (sec. 3.5), and correcting state evolution for nonlinear evolution due to nonharmonicities (sec. 3.6).

3.1 State preparation

As the first type of protocol, we consider state preparation. The initial state of the system is assumed to be the ground state $\psi_0(x)$ of the nonharmonic potential $v(x)$, well approximated by the wave function

$$\psi_0(x) \approx \frac{1}{\pi^{1/4}} e^{-x^2/2}, \quad (20)$$

which is the ground state of the leading harmonic approximation, $x^2/2$. For this protocol, we choose to control only the position of the potential $u(\tau)$, to maximize the fidelity

$$\mathcal{F} = |\langle \psi(x, \tau = \tau_{\max}) | \psi_T(x) \rangle|^2 \quad (21)$$

with the target state $\psi_T(x)$. We consider the preparation of several states, including Fock, finite GKP, cubic-phase, and cat states with high fidelity in a one-dimensional geometry. As these states are non-Gaussian, the role of nonharmonicity of the potential is evident—if it was quadratic, and dynamics linear, the Gaussianity of the state would be preserved during the evolution. In Fig. 1(b) we present an example of the excitation protocol, where we specialize to a Gaussian potential with $\eta = 0.25$. The target state is a finite GKP state,

$$\psi_{\text{GKP}}(x) = \mathcal{N} \sum_{i=1}^3 h_i e^{r/2} \psi_0[e^r(x - d_i)] \quad (22)$$

with $(h_1, h_2, h_3) = (1, 2, 1)$, $(d_1, d_2, d_3) = (-\sqrt{4\pi}, 0, \sqrt{4\pi})$, the squeezing parameter $r = 0.6$, the normalization constant \mathcal{N} , and the whole protocol is set to take $\tau_{\max}/2\pi = 6$. The presented protocol yields fidelity $\mathcal{F} \approx 99.8\%$. The further examples of the state preparation are presented in Fig. 2, both for the Gaussian potential and for cosine potential with the constraint (10), $\eta = 0.25$ and $d = 0.8$. Specifically, we additionally show the second excited Fock state,

$$\psi_2(x) = \frac{1}{\sqrt{2}} \frac{1}{\pi^{1/4}} (2x^2 - 1) e^{-x^2/2}, \quad (23)$$

the squeezed cubic-phase state,

$$\psi_{\text{cub}}(x) = e^{i\kappa x^3} e^{r/2} \psi_0(e^r x), \quad (24)$$

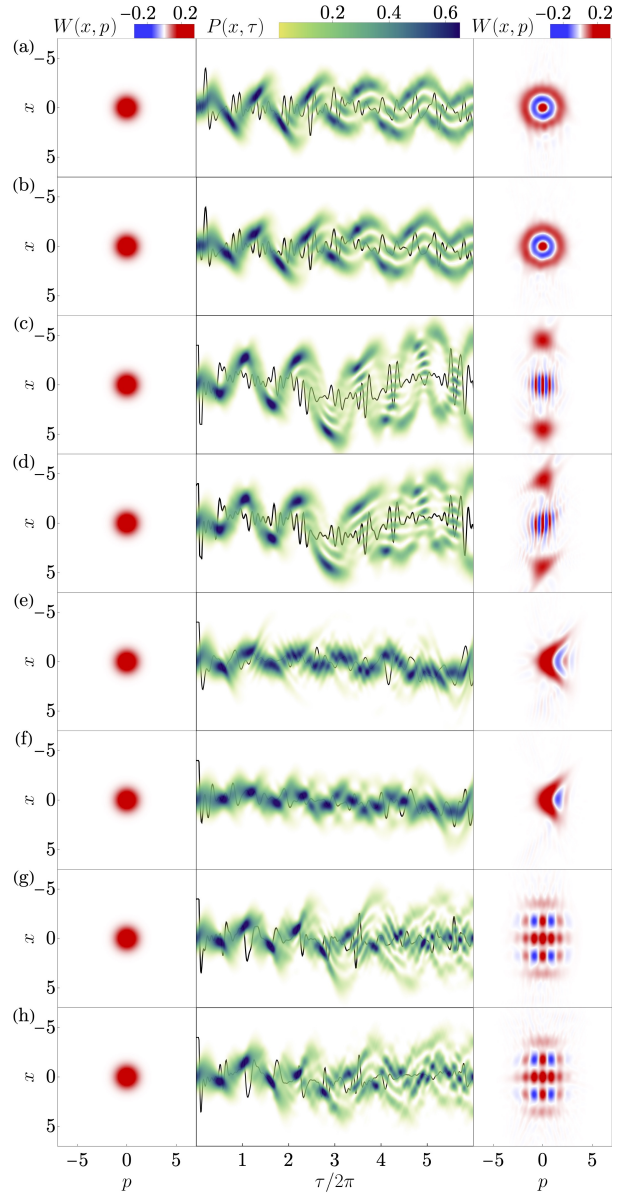


Figure 2: Examples of a state preparation protocol involving Gaussian [(a), (c), (e), (g)] and cosine [(b), (d), (f), (h)] single-well potentials, with $\eta = 0.25$ and $\tau_{\max}/2\pi = 6$, using only optimized position of the potential $u(\tau)$ in the case of the Gaussian potential. The protocols include second excited Fock [(a-b)], cat [(c-d), $s = 9$], cubic-phase [(e-f), $\kappa = 2$, $r = 0.7$], and GKP [(g-h), $r = 0.6$, $(d_1, d_2, d_3) = (-\sqrt{4\pi}, 0, \sqrt{4\pi})$, $(h_1, h_2, h_3) = (1, 2, 1)$] state preparation. Protocol fidelities \mathcal{F} are: (a) 99.8% (b) 99.8% (c) 92.7% (d) 93.4% (e) 97.2% (f) 94.9% (g) 99.8% (h) 99.8%.

and the cat state,

$$\psi_{\text{cat}}(x) = \frac{1}{\sqrt{2}} [\psi_0(x + s/2) + \psi_0(x - s/2)], \quad (25)$$

where κ is the cubicity, r is the squeezing parameter, and s is the separation between the coherent states. The specific values of the state parameters and fidelities are shown in the caption.

3.2 Unitaries

The next type of protocol involves the implementation of a specific unitary within a selected subspace. For simplicity and relevance to several proposals and realizations of bosonic qubits [13–17, 62, 101, 102], we analyze an example of a two-level subspace. This subspace can be spanned by any two orthogonal states $\psi^\pm(x)$, including two lowest-lying vibrational states $\psi_0(x)$ and $\psi_1(x)$ (Fock basis), two mutually displaced GKP states (GKP basis), four-, and two-legged-cat bases. For the protocol considered, the reward function is the subspace average gate fidelity [103]

$$\mathcal{F}_{\hat{U}} = \frac{1}{6}[\text{Tr}(\hat{M}\hat{M}^\dagger) + |\text{Tr} \hat{M}|^2], \quad (26)$$

where

$$\hat{M} = \hat{P}\hat{U}_T\hat{U}\hat{P}, \quad (27)$$

\hat{P} is a projector onto a subspace, \hat{U}_T is a target unitary, and \hat{U} is a unitary generated through Eq. (9). Taking advantage of the optimized position of the potential $u(\tau)$ and additional slight optimized modulation of the depth $a(\tau)$, we present examples of unitaries, e.g., σ_x or Hadamard operations, for above-mentioned subspaces. In Fig. 3(a,b) we show an exemplary case of four-legged-cat basis and σ_x operation performed with a Gaussian potential, where the basis states are given by

$$\psi_{4LC}^\pm(x) = \mathcal{N}_\pm [\varphi_\beta(x) + \varphi_{-\beta}(x) \pm \varphi_{i\beta}(x) \pm \varphi_{-i\beta}(x)], \quad (28)$$

respectively [104, 105]. Here, the coherent state reads

$$\varphi_\beta(x) = \frac{1}{\pi^{1/4}} \exp\left[-(x - \sqrt{2} \text{Re} \beta)^2/2 + i\sqrt{2}x \text{Im} \beta\right], \quad (29)$$

\mathcal{N}_\pm are the normalization constants, and we use $\beta = 2$. Again, the protocol is performed with high fidelity, $\mathcal{F}_{\hat{U}} \approx 99\%$. In Fig. 4 we show additional examples for Gaussian potential, including, among others, GKP basis, where the basis is spanned by two mutually displaced GKP states,

$$\psi^\pm = \psi_{\text{GKP}}(x \pm d_3/4), \quad (30)$$

where d_3 is defined as in (22) and the squeezing and displacement need to be enough for the states not to overlap. Further unitary implementations, but for the cosine potential with the constraint (10) are presented in the Appendix A.

3.3 Double-well potential landscape

Up to now, we have analyzed quantum dynamics taking place in a single well of a potential landscape. Here, we bring our attention to the nonharmonic potential landscape case that involves two independently

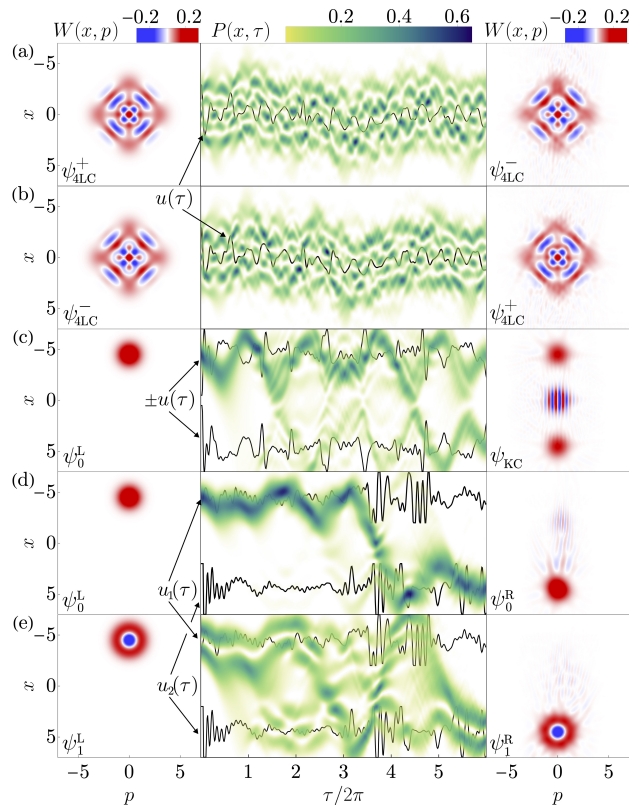


Figure 3: (a,b) Two orthogonal four-legged-cat states spanning a two-level subspace evolved in a position- and depth-controlled single Gaussian well, realizing a σ_x operation. (c) Cat state preparation using a double-well optimal control. The superscript L(R) signifies the state centered in the left(right) potential well. (d,e) State transfer between the wells—each of the vibrational states, $\psi_0(x)$ and $\psi_1(x)$, is transferred to the other well, without altering the relative phase.

controlled potential wells. Such a realization is available for optical lattices, optical tweezers [42, 77, 106–108], or various circuit quantum electrodynamics setups [109]. First, we address the state preparation and single-particle unitary implementation with two potential wells. We assume that we have two independently controlled wells at our disposal, such that the total potential reads

$$v(x) = \sum_{i=\{1,2\}} \frac{1}{2\eta^2} v_0[\eta(x - u_i(\tau))] \quad (31)$$

with two independent position control functions, $u_i(\tau)$. Here, we assume that v_0 contains only a single well with some characteristic width. Controlling the relative distance between the wells amounts to changing the barrier height, which affects the coupling between the bound states in each of the wells. It can be understood as mode multiplexing [110], accelerated through the optimal control. In Fig. 3(c), we show a balanced cat state preparation utilizing two Gaussian

potential wells,

$$\psi_0(x \pm s/2) \rightarrow \frac{1}{\sqrt{2}}[\psi_0(x \pm s/2) + i\psi_0(x \mp s/2)], \quad (32)$$

where s is the separation between the wells. Note that the presented control is symmetric, $u_1(\tau) = -u_2(\tau) = u(\tau)$, and the instantaneous separation between the wells is constrained in the optimization. The fidelity of the presented protocol yields $\mathcal{F} \approx 99\%$. The cat states produced in such a manner are pertinent to the fundamental tests of quantum mechanics, especially for massive objects. This protocol, along with a fast optimized transport [45], should allow for a fast macroscopic cat state creation and interferometric protocols.

The double-well potential has also been shown to provide a platform for fault-tolerant quantum computing with so-called Kerr-cats [15]. There, the computational subspace is spanned by superpositions of the ground states of the respective wells, corresponding to the (almost) degenerate ground-state manifold of a full double-well potential,

$$\psi_{\text{KC}}^{\pm}(x) = \frac{1}{\sqrt{2}}[\psi_0(x + s/2) \pm \psi_0(x - s/2)]. \quad (33)$$

With optimal control, one can again realize arbitrary unitaries within this subspace, utilizing the subspace average gate fidelity (26). Examples of σ_x , σ_y , and Hadamard unitaries are presented in detail in Appendix B. Furthermore, independent control of two wells can also be used to perform a state-preserving transport between the wells [111]. Here, the initial state is prepared within a two-dimensional subspace spanned by two orthogonal states localized in the left (L) well,

$$\psi_{\pm}^{\text{L}}(x) = \psi^{\pm}(x + s/2). \quad (34)$$

The aim of the protocol is to transfer such a state to a subspace localized in the right (R) well,

$$\psi_{\pm}^{\text{R}}(x) = \psi^{\pm}(x - s/2). \quad (35)$$

Then, if we introduce the following matrix,

$$\hat{M}' = \begin{pmatrix} \langle \psi_{+}^{\text{L}}(x, \tau_{\text{max}}) | \psi_{+}^{\text{R}}(x) \rangle & \langle \psi_{+}^{\text{L}}(x, \tau_{\text{max}}) | \psi_{-}^{\text{R}}(x) \rangle \\ \langle \psi_{-}^{\text{L}}(x, \tau_{\text{max}}) | \psi_{+}^{\text{R}}(x) \rangle & \langle \psi_{-}^{\text{L}}(x, \tau_{\text{max}}) | \psi_{-}^{\text{R}}(x) \rangle \end{pmatrix}, \quad (36)$$

where $\psi_{\pm}^{\text{L}}(x, \tau)$ is evolved according to the potential (31), we can define the state transfer fidelity,

$$\mathcal{F}_{\text{st}} = \frac{1}{6}[\text{Tr}(\hat{M}'\hat{M}'^{\dagger}) + |\text{Tr}\hat{M}'|^2], \quad (37)$$

as the reward function. In Fig. 3(d,e) we show the example of a state of two lowest vibrational levels of the left well transferred to the right one with $\mathcal{F}_{\text{st}} \approx 99\%$.

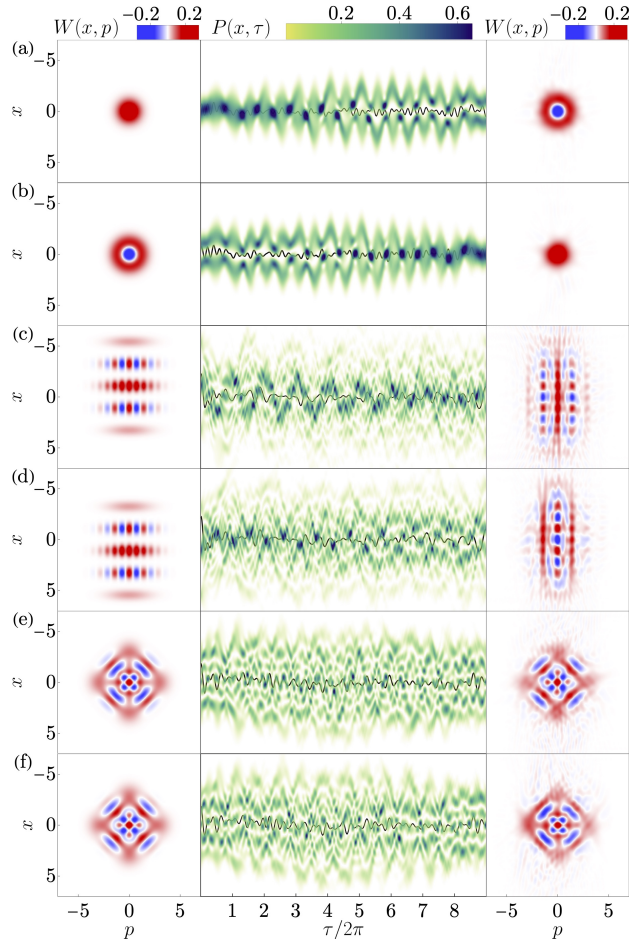


Figure 4: Evolution of selected orthogonal states in a Gaussian potential characterized by $\eta = 0.25$ and with optimally controlled displacement $u(\tau)$ and intensity $a(\tau)$. The solid line shows $u(\tau)$ and the protocol lasts $\tau_{\text{max}}/2\pi = 9$. (a-b) σ_x unitary within a subspace spanned by ψ_0 and ψ_1 Fock states. The fidelity reads $\mathcal{F}_{\hat{U}} \approx 99.8\%$. (c-d) Hadamard unitary within a subspace spanned by GKP states with $r = 0.7$, $(d_1, d_2, d_3) = (-\sqrt{6\pi}, 0, \sqrt{6\pi})$. The fidelity reads $\mathcal{F}_{\hat{U}} \approx 96.4\%$. (e-f) σ_y unitary within a subspace spanned by four-legged-cat states with $\beta = 2$. The fidelity reads $\mathcal{F}_{\hat{U}} \approx 96.2\%$.

3.4 Single-shot discrimination

After presenting state preparation and unitary implementation in various nonharmonic potential landscapes, we move on to two protocols that perform single-shot discrimination between two orthogonal states $\psi^{\pm}(x)$ (see Fig. 5), providing an alternative to already existing methods involving auxiliary systems in, e.g., superconducting circuits [36]. The first one involves a single nonharmonic well and is performed through imprinting opposite momentum kicks onto each of the states via a potential displacement,

$$\psi^{\pm}(x) \rightarrow \psi_k^{\pm}(x) = \psi^{\pm}(x)e^{\pm ikx}, \quad (38)$$

where k is chosen such that two phase-imprinted states are nonoverlapping in phase space. After

the phase imprinting, a selective measurement takes place, which can be realized in, e.g., optical tweezer setup through the subsequent release of the trap in which time-of-flight evolution reveals spatially separated detection clicks for each of the states [44, 112]. The reward function for such a momentum-kick protocol involves a sum of an equally weighted fidelities,

$$\mathcal{F}_{\text{mk}} = \frac{1}{2} \sum_{j=\pm} \left| \langle \psi^j(x, \tau_{\text{max}}) | \psi_k^j(x) \rangle \right|^2 \quad (39)$$

Note that in contrast to the unitary implementation, here the final relative phase between the states does not matter, as we aim only to distinguish the initial states. As an example, in Fig. 5 $\psi^\pm(x)$ are taken to be the two lowest eigenstates of the well and the protocol is shown in the schematic way. In Fig. 6 we show in detail specific realizations of this and other momentum-kick protocols, utilizing a double-well Gaussian potential. They involve also other choices of orthogonal states for the discrimination, namely eigenstates of both σ_x and σ_y Pauli matrices. Such discrimination procedures then correspond to σ_x and σ_y measurements within a given two-level subspace.

The second discrimination protocol involves a double-well potential landscape and utilizes spatial separation instead of the momentum one (see Fig. 5). Initially, the states are fully confined to the left well and their discrimination is realized through a selective stealing protocol—if the state is $\psi^+(x)$, then it ends up in the second well after the optimal shaking, while $\psi^-(x)$ stays in the initial one. Then, large spatial separation between the wells enables selective measurement. The reward function for this protocol, the selective-stealing fidelity, reads

$$\mathcal{F}_{\text{ss}} = \frac{1}{2} \left[\left| \langle \psi_-^{\text{L}}(x, \tau_{\text{max}}) | \psi_-^{\text{L}}(x) \rangle \right|^2 + \left| \langle \psi_+^{\text{L}}(x, \tau_{\text{max}}) | \psi_+^{\text{R}}(x) \rangle \right|^2 \right], \quad (40)$$

where the definitions (34) and (35) are used. We show the exemplary case of distinguishing two lowest vibrational states in two top panels of Fig. 7, while further examples, including discrimination of σ_x and σ_y eigenstates, are presented in Appendix C.

3.5 Cooling

These methods performed on low-lying eigenstates of a nonharmonic well can be straightforwardly extended into cooling protocols, similar to algorithmic [38, 39] or evaporative cooling. These protocols involve bringing not only the first excited state $\psi_1(x)$ but also higher excited states $\psi_n(x)$ into a second potential well or kicking them out of the well, followed by the destructive measurement of the separated excited fraction. In the former case, the reward function reads

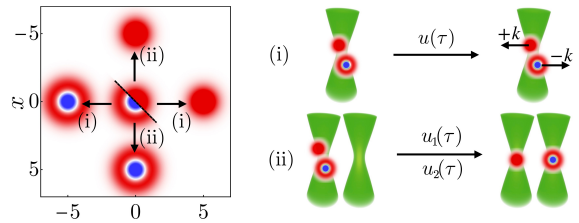


Figure 5: Two proposed discrimination protocols, based on a phase-space separation. (i) The opposite momentum kicks are imprinted onto each of the states. (ii) States are separated spatially via a second potential well.

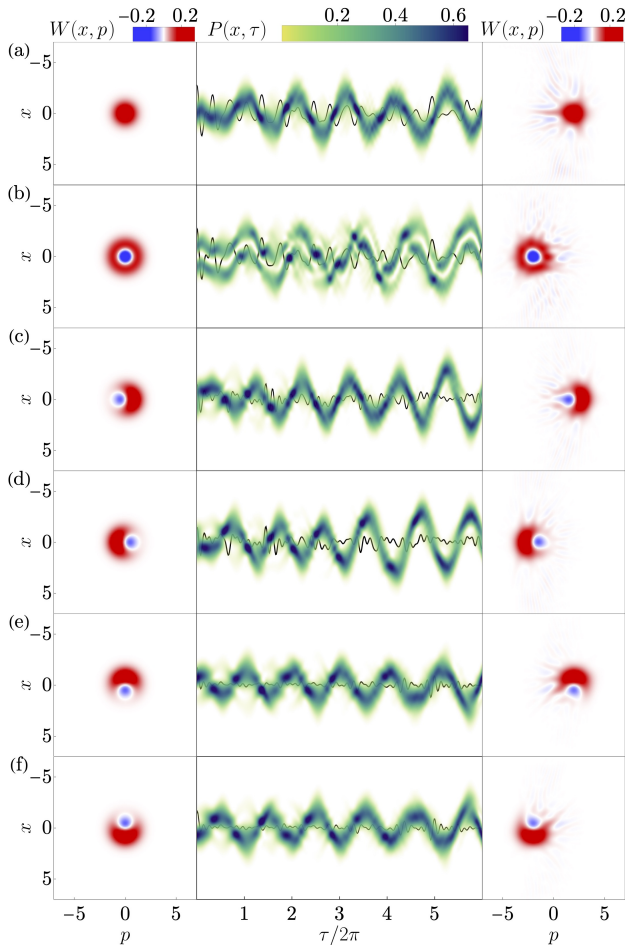


Figure 6: Examples of the implementation of momentum kick protocols via an optimally controlled single-well Gaussian potential with $\eta = 0.25$, $\tau_{\text{max}}/2\pi = 6$, and $k = 2$. (a-b) $\psi^+(x) = \psi_0(x)$ and $\psi^-(x) = \psi_1(x)$, (c-d) $\psi^\pm(x) = [\psi_0(x) \pm \psi_1(x)]/\sqrt{2}$, and (e-f) $\psi^\pm(x) = [\psi_0(x) \pm i\psi_1(x)]/\sqrt{2}$. Momentum-kick fidelities read (a-b) $\mathcal{F}_{\text{mk}} \approx 98.5\%$, (c-d) $\mathcal{F}_{\text{mk}} \approx 99.4\%$, and (e-f) $\mathcal{F}_{\text{mk}} \approx 99.5\%$.

$$\mathcal{F}_{\text{ss}}^{\text{cool}} = \frac{1}{N+1} \left[\left| \langle \psi_0^{\text{L}}(x, \tau_{\text{max}}) | \psi_0^{\text{L}}(x) \rangle \right|^2 + \sum_{n=1}^N \left| \langle \psi_n^{\text{L}}(x, \tau_{\text{max}}) | \psi_n^{\text{R}}(x) \rangle \right|^2 \right], \quad (41)$$

where

$$\begin{aligned}\psi_n^L(x) &= \psi_n(x + s/2), \\ \psi_n^R(x) &= \psi_n(x - s/2).\end{aligned}\quad (42)$$

Here, N characterizes the amount of excited states that are brought to the other well. The higher N , the more thermal state can be brought to the ground state. However, higher temperature also means a lower chance of success, as the presence of the ground state in the left well is conditioned on the subsequent destructive measurement in the right well. Hence, on average, the success rate of the protocol is proportional to the initial occupation of the ground state. Fig. 7 demonstrates this process for the four lowest states of the well, with the higher three states becoming spatially separated from the ground state. The method involving momentum-kick protocol is analogous, but with the excited fraction being kicked out of the well. The reward function is thus

$$\begin{aligned}\mathcal{F}_{\text{mk}}^{\text{cool}} &= \frac{1}{N+1} \left[|\langle \psi_0(x, \tau_{\text{max}}) | \psi_0(x) \rangle|^2 \right. \\ &\quad \left. + \sum_{n=1}^N |\langle \psi_n(x, \tau_{\text{max}}) | \psi_n^k(x) \rangle|^2 \right],\end{aligned}\quad (43)$$

where

$$\psi_n^k(x) = e^{ikx} \psi_n(x).\quad (44)$$

3.6 State stabilization

Note that undriven evolution is nonlinear and hence, the prepared state gets distorted during the evolution. In contrast, when evolved in the perfectly harmonic potential, the state undergoes rotation in the phase space with the trap period. In a realistic setup, such a state preservation in the rotating frame is destroyed by the nonharmonicity of the potential. The remedy lies in either decreasing the nonharmonicity or, alternatively, mimicking perfect phase space rotation through optimal control [60]. We present the latter method, which consists of two optimization steps. The first one involves using the average fidelity with respect to the perfectly rotating state during a multiple of the trap period $\tau_{\text{max}} = n2\pi$ as a reward function,

$$\mathcal{F}_{\text{rot}} = \frac{1}{\tau_{\text{max}}} \int d\tau |\langle \psi(x, \tau) | \psi_{\text{rot}}(x, \tau) \rangle|^2,\quad (45)$$

where

$$|\psi_{\text{rot}}(\tau)\rangle = e^{-i\hat{a}^\dagger \hat{a} \tau} |\psi(0)\rangle\quad (46)$$

is the initial state undergoing a phase-space rotation in a perfectly harmonic trap. After optimizing \mathcal{F}_{rot} , the next step involves maximizing the final fidelity with the initial state after a single trap period,

$$\mathcal{F} = |\langle \psi(x, \tau_{\text{max}}) | \psi(x, 0) \rangle|^2.\quad (47)$$

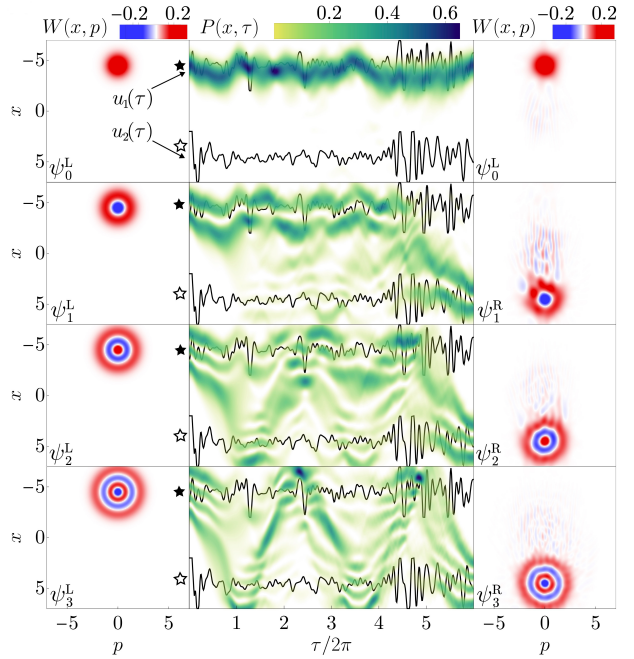


Figure 7: The accelerated algorithmic cooling method by spatial separation of the ground and excited fractions realized through optimal control of two wells. The selective-stealing cooling fidelity reads $\mathcal{F}_{\text{ss}}^{\text{cool}} \approx 97\%$.

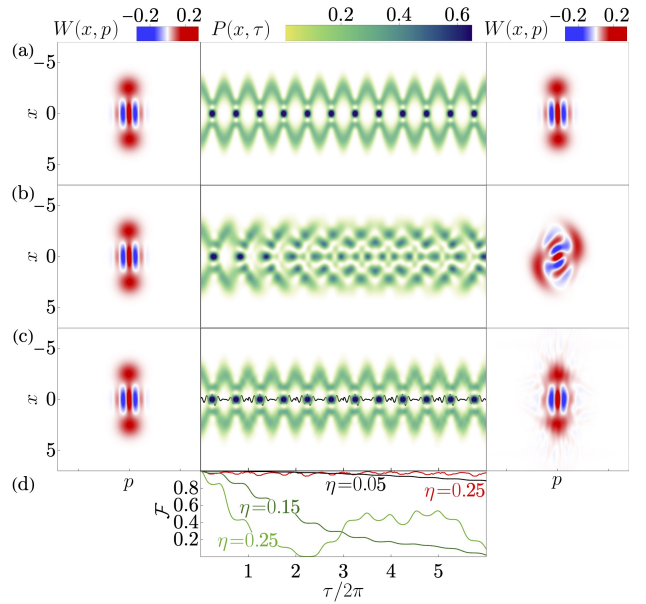


Figure 8: (a) Temporal evolution of a cat state in a perfectly harmonic potential. It rotates in the phase space and fully revives every trap period. (b) Evolution of a cat state in a tweezer characterized by $\eta = 0.25$. (c) Evolution of a cat state in a tweezer characterized by $\eta = 0.25$, however with optimally controlled potential position and depth. (d) Fidelities between a cat state rotating in a perfectly harmonic potential and in Gaussian potentials with different nonharmonicities without (shades of green) and with (red) optimal control.

The second step guarantees high fidelity, should the protocol be applied consecutively many times, while the first one ensures that state is not distorted at any time. In Fig. 8 we present an example of an optimally controlled cat state stabilization. The optimization is conducted for a single trap period, $\tau_{\max} = 2\pi$ with both position and depth control of a Gaussian potential. Subsequently, the optimized control is applied six times consecutively over six trap periods and compared with the bare evolution in a Gaussian potential. The results showcase that the presented optimal stabilization of the state surpasses that of a Gaussian potential with a relatively low nonharmonicity $\eta = 0.05$, within this particular time scale.

4 Feasibility

After presenting several protocols, let us now address aspects relevant to their experimental implementation. From now on, we will focus on the Fock state preparation protocol with a single-well Gaussian potential as an exemplary case. In subsection 4.1 we analyze how fast the optimized protocol can be and how excited the system is during its evolution. Then, in subsection 4.2 we check the robustness of the state preparation in the presence of noise and decoherence modeled by the stochastic fluctuations of the potential. Finally, subsection 4.3 addresses the issue of satisfying one-dimensional approximation in the specific case of an atom in an optical tweezer.

4.1 Quantum speed limit

Concerning the protocol's speed, a fundamental restriction exists, the quantum speed limit [113], which gives the minimal time that is needed to perform a specific state transfer with a given fidelity threshold. Well-understood for two-level systems driven by static Hamiltonians [113–115], quantum speed limits have also been analyzed for time-dependent multilevel systems [116, 117], and, specifically, for the ground to the first excited state transfer in a Bose-Einstein condensate [51]. We analyze a Gaussian potential case to find a minimum time τ_{QSL} needed to perform the excitation from the ground to the first excited state, $\psi_0(x) \rightarrow \psi_1(x)$, with some infidelity threshold for different values of nonharmonicity η . In the regime of interest, $\eta \sim 0.1 - 0.5$, there is no strong scaling of τ_{QSL} with the nonharmonicity and achievable fidelity scales exponentially with the protocol time. For the example of an optical tweezer, it implies that, without noise, the deeper the tweezer, the more bound states accessed and the faster the protocol (and hence requiring more control bandwidth), as $\omega \sim V_0^{1/2}$. We then analyze the number of excitations averaged throughout the protocol,

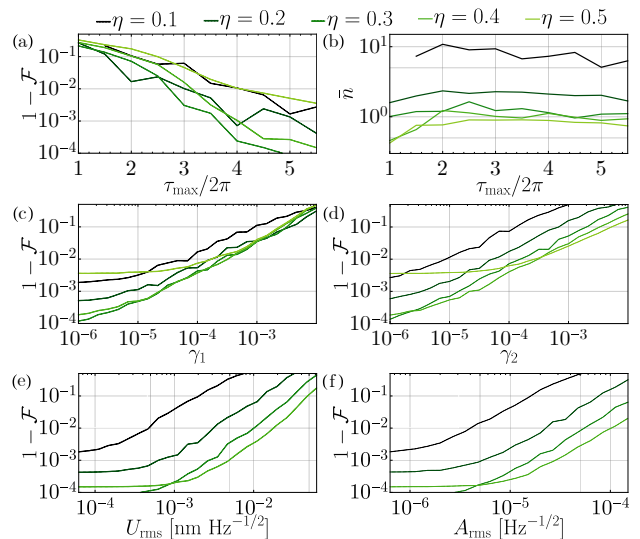


Figure 9: (a) Infidelity of the ground to the first excited state transfer, $\psi_0(x) \rightarrow \psi_1(x)$, for a Gaussian potential as a function of the length of protocol τ_{\max} and nonharmonicity η . The scaling of the curve is as expected from the previous studies [51] and reveals that a quantum speed limit τ_{QSL} does not scale strongly with η . (b) Average excitation number as a function of τ_{\max} and η . (c,d) The minimal achievable infidelity for given values of position (γ_1) and depth (γ_2) noises for a Gaussian potential. (e,f) The minimal achievable infidelity for given values of displacement U_{rms} and intensity A_{rms} noises for a rubidium-87 atom in an optical tweezer with the waist $w_0 = 710$ nm. The value of nonharmonicity η is tuned via the tweezer's depth V_0 .

$$\bar{n} = \int d\tau \sum_n n |c_n(\tau)|^2, \quad (48)$$

as it is relevant for analytical quantum speed limits [115, 118, 119] and proneness to decoherence. Fig. 9(b) shows the results, displaying an increase of the average excitation number with decreasing nonharmonicity, indicating that more nonharmonic potentials are preferred when low excitation is necessitated.

4.2 Noise and decoherence

Let us now address the noise robustness of the state preparation protocols. In general, for different experimental realizations, typical sources of error include stochastic vibrations of the potential, low-frequency drifts between experimental runs, imperfections of the control, etc. To model potential vibrations and control imperfections in a single potential well, we employ stochastic fluctuations of the depth and position of the potential,

$$\begin{aligned} a(\tau) &\rightarrow a(\tau) + \xi_2(\tau), \\ u(\tau) &\rightarrow u(\tau) + \xi_1(\tau), \end{aligned} \quad (49)$$

where $\xi_j(\tau)$ for $j = 1, 2$ are dimensionless stochastic Gaussian variables of zero mean and assumed delta-

correlated in the relevant time scales, namely

$$\langle \xi_j(\tau)\xi_j(\tau') \rangle = \gamma_j \delta(\tau - \tau'). \quad (50)$$

We solve noisy dynamics by averaging over different noise realizations and constructing a Monte Carlo density matrix [120]. In Figs. 9(c,d) we plot the minimal achievable infidelity at a given level of noise for the ground to the first excited state excitation protocol for a single Gaussian potential. While the positional noise affects the protocol comparably for each η , the depth noise influences the strongest the least nonharmonic case. For the specific mapping onto pointing and intensity noise in an optical tweezer setup, we have

$$\begin{aligned} \gamma_1 &= \frac{U_{\text{rms}}^2 \omega}{X_0^2}, \\ \gamma_2 &= A_{\text{rms}}^2 \omega, \end{aligned} \quad (51)$$

where U_{rms} is a pointing root mean square (RMS) noise, and A_{rms} is an intensity RMS noise. In Figs. 9(e,f) we plot the fidelity loss as a function of U_{rms} and A_{rms} , and we find that shallower (more non-harmonic) tweezers outperform the deeper ones.

4.3 Coherent couplings

Coherent coupling to other degrees of freedom might cause an additional experimental challenge. The exemplary case of such a noisy channel occurs in one of the setups we consider and is due to the dimensionality of the realistic optical potential. The three-dimensional tweezer potential is necessarily nonseparable and, depending on the axis of control, axial or radial, a one-dimensional approximation may be less strictly satisfied [121]. Restricting control to only one direction unavoidably leads to excitation in other ones. However, the fidelity loss due to these excitations can be alleviated through additional optimization in fully three-dimensional potential and additional optimized position and depth controls. The additional control then effectively deexcites the coupled degrees of freedom. This optimization can be done via a staged procedure, where the initial guess for a higher-dimensional system comes from a reduced-dimensional control optimization. Such an optimization procedure can be utilized in setups in which coherent dynamics beyond one-dimensional approximation can be solved.

Here we present the analysis of the Fock $\psi_1(x)$ state preparation protocol in the two- and three-dimensional geometry. The dynamics is driven by either two-dimensional,

$$\begin{aligned} v_{2\text{D}}(x, y) &= \frac{3}{4\eta^2} \left[1 - \exp\left(-\frac{2}{3}\eta^2(x^2 + y^2)\right) \right] \\ &\approx \frac{1}{2}x^2 + \frac{1}{2}y^2, \end{aligned} \quad (52)$$

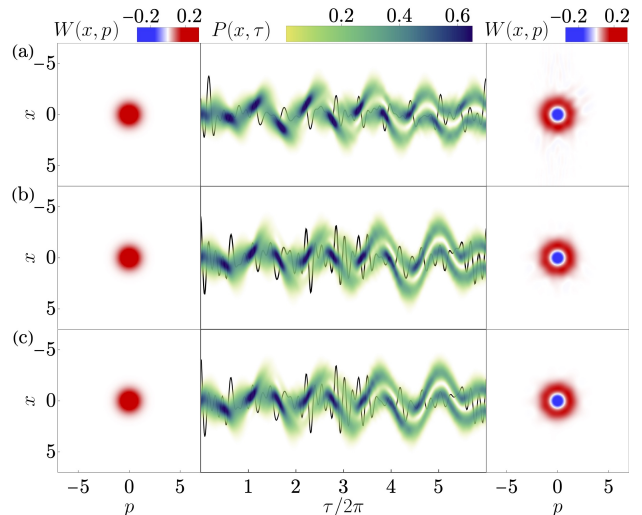


Figure 10: Fock $\psi_1(x)$ state preparation protocol with the optimally controlled Gaussian potential characterized with $\eta = 0.25$ and $\lambda = 0.167$ for (a) one-, (b) two-, and (c) three-dimensional geometries. Achieved fidelities \mathcal{F} read (a) 99.7%, (b) 99.4%, and (c) 99.0%.

or three-dimensional Gaussian potential,

$$\begin{aligned} v_{3\text{D}}(x, y, z) &= \frac{3}{4\eta^2} \frac{1 + \frac{2}{3}\eta^2\lambda^2 z^2 - \exp\left[-\frac{2}{3}\frac{\eta^2(x^2 + y^2)}{1 + \frac{2}{3}\eta^2\lambda^2 z^2}\right]}{1 + \frac{2}{3}\eta^2\lambda^2 z^2}, \\ &\approx \frac{1}{2}x^2 + \frac{1}{2}y^2 + \frac{1}{2}\lambda^2 z^2 \end{aligned} \quad (53)$$

where λ is the aspect ratio between the radial and axial trapping frequencies, $\lambda = \omega/\omega_{\text{ax}}$, and the leading harmonic approximations are given. The initial states are taken to be the ground states of the harmonic approximations,

$$\begin{aligned} \psi_0(x, y) &= \psi_0(x)\psi_0(y), \\ \psi_0(x, y, z) &= \psi_0(x)\psi_0(y)\lambda^{1/4}\psi_0(\lambda z). \end{aligned} \quad (54)$$

The control $u(\tau)$ is taken to be only x -displacement,

$$\begin{aligned} v_{2\text{D}}(x, y, \tau) &= v_{2\text{D}}[x - u(\tau), y], \\ v_{3\text{D}}(x, y, z, \tau) &= v_{3\text{D}}[x - u(\tau), y, z], \end{aligned} \quad (55)$$

and optimized through a staged procedure: the optimized control in the one-dimensional problem is a starting guess for the two-dimensional control; analogously for the three-dimensional case. In Fig. 10 we plot the results of such an optimization with the snapshots of Wigner functions associated with reduced density matrices,

$$\begin{aligned} \hat{\rho}_{2\text{D}} &= \text{Tr}_y \hat{\rho}, \\ \hat{\rho}_{3\text{D}} &= \text{Tr}_{y,z} \hat{\rho}, \end{aligned} \quad (56)$$

for two- and three-dimensional cases, respectively. Here, $\hat{\rho}$ is the full motional density matrix. As for the low-frequency drifts, one can further optimize the control functions in the presence of varying experimental

parameters, a commonly utilized technique [35]. Going beyond the single-well case, note that arbitrary control of double-well systems can lead to additional sources of noise, including, e.g., relative bias fluctuations.

5 Conclusions & outlook

In conclusion, we have presented an approach that allows the preparation and manipulation of a state of a single continuous-variable degree of freedom and relies only on self-contained nonlinear dynamics without any additional nonlinear couplings. Specifically, the presented method utilizes optimal control of the intrinsic nonharmonicity present in the effective confining potential, a common scenario in many continuous-variable systems, including neutral atoms in optical tweezers and lattices or flux-tunable transmons. We have presented quantum state preparation, implementation of arbitrary unitaries within a selected subspace, quantum discrimination protocols based on phase-space separation, algorithmic cooling, spatial logical state transfer, and protection from state deformation during nonlinear dynamics that can be realized in such systems. We have shown that these protocols can be performed via both single- and double-well potential landscapes. The protocols that we have proposed are particularly well-suited for systems in which coherent couplings to two-level degrees of freedom have not been realized. Beyond such systems, they can be implemented in setups with already well-developed quantum control, such as superconducting circuits, either as a proof of principle, as an addition to an already existing experimental toolbox, or as a way to unify the utilization of different types of quantum non-Gaussian states.

Moreover, we have analyzed the performance of the state preparation protocols, from the perspective of the speed of the protocols, under the effect of position and depth noises, and with additional coherent couplings. These aspects have been checked for a specific example of an atom in an optical tweezer. Our proposal is compatible with state-of-the-art technology, such as neutral atoms, circuit quantum electrodynamics, or Bose-Einstein condensates, and might be explored in systems with smaller nonharmonicities, e.g., levitated nanoparticles ($\eta \sim 10^{-5}$) [84, 85] or ions in Paul traps (typically $\eta \sim 10^{-2} - 10^{-1}$, which allows a crossover between weak and strong nonharmonicity) [24, 83]. More specifically, for the tasks we consider, controllability decreases with decreasing nonharmonicity, confirming notorious difficulty in preparing non-Gaussian states in weakly nonharmonic systems. The strategies to circumvent this problem involve large excitation of involved states through, e.g., phase-displacement in cavities for Fock state preparation [86, 87] or motional squeezing in mechanical oscillators for cubic- [85, 122, 123] and quartic-

phase state preparation [124]. Combining optimal control of the potential landscape with such a nonharmonicity enhancement may bring these weakly nonharmonic systems closer to universal quantum control in a resource-optimal way.

Data and materials availability

The Fourier transforms of all presented controls are presented in Appendix D, while the depth modulations not shown in the main text are plotted in Appendix E. Data analysis and simulation codes are available on Zenodo upon reasonable request [125].

Acknowledgments

We thank R. G. Cortiñas, N. E. Frattini, S. Muleady, A. M. Rey, and P. Zoller for helpful discussions. The computational results presented here have been achieved in part using the LEO HPC infrastructure of the University of Innsbruck. P.T.G. and O.R.-I. have been supported by the European Union’s Horizon 2020 research and innovation programme under grant agreement No. 863132 (IQLev) and by the European Research Council (ERC) under the grant agreement No. 951234 (Q-Xtreme ERC-2020-SyG). P.T.G. was partially supported by the project CZ.02.01.01/00/22_008/0004649 (QUEENTEC) of EU. H.P. has been supported through an ERC Starting grant QARA (grant no. 101041435) and the European Union’s Horizon 2020 research and innovation program under Grant Agreement No. 101079862 (PASQuanS2). C.A.R. has been supported by NSF PHY-2317149, NSF QLCI award OMA 2016244, the US Department of Energy, Office of Science, National Quantum Information Science Research Centers, Quantum Systems Accelerator, and the Baur-SPIE Chair at JILA.

References

- [1] W. H. Zurek, “Sub-Planck structure in phase space and its relevance for quantum decoherence,” *Nature* **412**, 712–717 (2001).
- [2] S. Deléglise, I. Dotsenko, C. Sayrin, J. Bernu, M. Brune, J.-M. Raimond, and S. Haroche, “Reconstruction of non-classical cavity field states with snapshots of their decoherence,” *Nature* **455**, 510–514 (2008).
- [3] M. Arndt, O. Nairz, J. Vos-Andreae, C. Keller, G. van der Zouw, and A. Zeilinger, “Wave-particle duality of C60 molecules,” *Nature* **401**, 680–682 (1999).
- [4] Y. Y. Fein, P. Geyer, P. Zwick, F. Kiałka, S. Pedalino, M. Mayor, S. Gerlich, and M. Arndt, “Quantum superposition of molecules

- beyond 25 kDa,” *Nat. Phys.* **15**, 1242–1245 (2019).
- [5] M. Bild, M. Fadel, Y. Yang, U. von Lüpke, P. Martin, A. Bruno, and Y. Chu, “Schrödinger cat states of a 16-microgram mechanical oscillator,” *Science* **380**, 274–278 (2023).
- [6] A. Peters, K. Y. Chung, and S. Chu, “High-precision gravity measurements using atom interferometry,” *Metrologia* **38**, 25 (2001).
- [7] P. W. Graham, J. M. Hogan, M. A. Kasevich, and S. Rajendran, “New Method for Gravitational Wave Detection with Atomic Sensors,” *Phys. Rev. Lett.* **110**, 171102 (2013).
- [8] R. H. Parker, C. Yu, W. Zhong, B. Estey, and H. Müller, “Measurement of the fine-structure constant as a test of the Standard Model,” *Science* **360**, 191–195 (2018).
- [9] Y. Margalit, O. Dobkowski, Z. Zhou, O. Amit, Y. Japha, S. Moukouri, D. Rohrlach, A. Mazumdar, S. Bose, C. Henkel, and R. Folman, “Realization of a complete Stern-Gerlach interferometer: Toward a test of quantum gravity,” *Sci. Adv.* **7**, eabg2879 (2021).
- [10] D. Gottesman, A. Kitaev, and J. Preskill, “Encoding a qubit in an oscillator,” *Phys. Rev. A* **64**, 012310 (2001).
- [11] E. Knill, R. Laflamme, and G. J. Milburn, “A scheme for efficient quantum computation with linear optics,” *Nature* **409**, 46–52 (2001).
- [12] R. W. Heeres, P. Reinhold, N. Ofek, L. Frunzio, L. Jiang, M. H. Devoret, and R. J. Schoelkopf, “Implementing a universal gate set on a logical qubit encoded in an oscillator,” *Nat. Commun.* **8**, 94 (2017).
- [13] P. Reinhold, S. Rosenblum, W.-L. Ma, L. Frunzio, L. Jiang, and R. J. Schoelkopf, “Error-corrected gates on an encoded qubit,” *Nat. Phys.* **16**, 822–826 (2020).
- [14] Y. Ma, Y. Xu, X. Mu, W. Cai, L. Hu, W. Wang, X. Pan, H. Wang, Y. P. Song, C.-L. Zou, and L. Sun, “Error-transparent operations on a logical qubit protected by quantum error correction,” *Nat. Phys.* **16**, 827–831 (2020).
- [15] A. Grimm, N. E. Frattini, S. Puri, S. O. Mundhada, S. Touzard, M. Mirrahimi, S. M. Girvin, S. Shankar, and M. H. Devoret, “Stabilization and operation of a Kerr-cat qubit,” *Nature* **584**, 205–209 (2020).
- [16] J. M. Gertler, B. Baker, J. Li, S. Shirol, J. Koch, and C. Wang, “Protecting a bosonic qubit with autonomous quantum error correction,” *Nature* **590**, 243–248 (2021).
- [17] B. de Neeve, T.-L. Nguyen, T. Behrle, and J. P. Home, “Error correction of a logical grid state qubit by dissipative pumping,” *Nat. Phys.* **18**, 296–300 (2022).
- [18] D. González-Cuadra, D. Bluvstein, M. Kalinowski, R. Kaubuegger, N. Maskara, P. Naldesi, T. V. Zache, A. M. Kaufman, M. D. Lukin, H. Pichler, B. Vermersch, J. Ye, and P. Zoller, “Fermionic quantum processing with programmable neutral atom arrays,” *Proc. Natl. Acad. Sci. U.S.A.* **120**, e2304294120 (2023).
- [19] J. I. Cirac, A. S. Parkins, R. Blatt, and P. Zoller, “Nonclassical States of Motion in Ion Traps,” in *Advances In Atomic, Molecular, and Optical Physics*, Vol. 37, edited by B. Bederson and H. Walther (Academic Press, 1996) pp. 237–296.
- [20] D. M. Meekhof, C. Monroe, B. E. King, W. M. Itano, and D. J. Wineland, “Generation of Nonclassical Motional States of a Trapped Atom,” *Phys. Rev. Lett.* **76**, 1796–1799 (1996).
- [21] J. C. Loredó, C. Antón, B. Reznichenko, P. Hilaire, A. Harouri, C. Millet, H. Ollivier, N. Somaschi, L. De Santis, A. Lemaître, I. Sagnes, L. Lanco, A. Auffèves, O. Krebs, and P. Senellart, “Generation of non-classical light in a photon-number superposition,” *Nat. Photonics* **13**, 803–808 (2019).
- [22] R. Trivedi, K. A. Fischer, J. Vučković, and K. Müller, “Generation of Non-Classical Light Using Semiconductor Quantum Dots,” *Adv. Quantum Technol.* **3**, 1900007 (2020).
- [23] R. Jáuregui, N. Poli, G. Roati, and G. Modugno, “Anharmonic parametric excitation in optical lattices,” *Phys. Rev. A* **64**, 033403 (2001).
- [24] J. P. Home, D. Hanneke, J. D. Jost, D. Leibfried, and D. J. Wineland, “Normal modes of trapped ions in the presence of anharmonic trap potentials,” *New J. Phys.* **13**, 073026 (2011).
- [25] A. Blais, A. L. Grimsmo, S. M. Girvin, and A. Wallraff, “Circuit quantum electrodynamics,” *Rev. Mod. Phys.* **93**, 025005 (2021).
- [26] J. Gorman, D. G. Hasko, and D. A. Williams, “Charge-Qubit Operation of an Isolated Double Quantum Dot,” *Phys. Rev. Lett.* **95**, 090502 (2005).
- [27] C. Gollub, U. Troppmann, and R. de Vivie-Riedle, “The role of anharmonicity and coupling in quantum computing based on vibrational qubits,” *New J. Phys.* **8**, 48 (2006).
- [28] J. Koch, T. M. Yu, J. Gambetta, A. A. Houck, D. I. Schuster, J. Majer, A. Blais, M. H. Devoret, S. M. Girvin, and R. J. Schoelkopf, “Charge-insensitive qubit design derived from the Cooper pair box,” *Phys. Rev. A* **76**, 042319 (2007).
- [29] J. A. Schreier, A. A. Houck, J. Koch, D. I. Schuster, B. R. Johnson, J. M. Chow, J. M. Gambetta, J. Majer, L. Frunzio, M. H. Devoret, S. M. Girvin, and R. J. Schoelkopf, “Suppressing charge noise decoherence in superconducting charge qubits,” *Phys. Rev. B* **77**, 180502 (2008).

- [30] F. Pistolesi, A. N. Cleland, and A. Bachtold, “Proposal for a Nanomechanical Qubit,” *Phys. Rev. X* **11**, 031027 (2021).
- [31] Z. Leghtas, G. Kirchmair, B. Vlastakis, R. J. Schoelkopf, M. H. Devoret, and M. Mirrahimi, “Hardware-Efficient Autonomous Quantum Memory Protection,” *Phys. Rev. Lett.* **111**, 120501 (2013).
- [32] Y. Zheng, O. Hahn, P. Stadler, P. Holmvall, F. Quijandría, A. Ferraro, and G. Ferrini, “Gaussian Conversion Protocols for Cubic Phase State Generation,” *PRX Quantum* **2**, 010327 (2021).
- [33] S. J. Glaser, U. Boscain, T. Calarco, C. P. Koch, W. Köckenberger, R. Kosloff, I. Kuprov, B. Luy, S. Schirmer, T. Schulte-Herbrüggen, D. Sugny, and F. K. Wilhelm, “Training Schrödinger’s cat: Quantum optimal control,” *Eur. Phys. J. D* **69**, 279 (2015).
- [34] C. P. Koch, U. Boscain, T. Calarco, G. Dirr, S. Filipp, S. J. Glaser, R. Kosloff, S. Montangero, T. Schulte-Herbrüggen, D. Sugny, and F. K. Wilhelm, “Quantum optimal control in quantum technologies. Strategic report on current status, visions and goals for research in Europe,” *EPJ Quantum Technol.* **9**, 1–60 (2022).
- [35] M. Rossignolo, T. Reisser, A. Marshall, P. Rembold, A. Pagano, P. J. Vetter, R. S. Said, M. M. Müller, F. Motzoi, T. Calarco, F. Jelezko, and S. Montangero, “QuOCS: The quantum optimal control suite,” *Comput. Phys. Commun.* **291**, 108782 (2023).
- [36] D. I. Schuster, A. A. Houck, J. A. Schreier, A. Wallraff, J. M. Gambetta, A. Blais, L. Frunzio, J. Majer, B. Johnson, M. H. Devoret, S. M. Girvin, and R. J. Schoelkopf, “Resolving photon number states in a superconducting circuit,” *Nature* **445**, 515–518 (2007).
- [37] M. Mallweger, M. H. de Oliveira, R. Thomm, H. Parke, N. Kuk, G. Higgins, R. Bachelard, C. J. Villas-Boas, and M. Hennrich, “Single-Shot Measurements of Phonon Number States Using the Autler-Townes Effect,” *Phys. Rev. Lett.* **131**, 223603 (2023).
- [38] M. Popp, J.-J. Garcia-Ripoll, K. G. H. Vollbrecht, and J. I. Cirac, “Cooling toolbox for atoms in optical lattices,” *New J. Phys.* **8**, 164 (2006).
- [39] A. L. Shaw, P. Scholl, R. Finkelstein, R. B.-S. Tsai, J. Choi, and M. Endres, “Erasure-cooling, control, and hyper-entanglement of motion in optical tweezers,” *arXiv:2311.15580* (2023).
- [40] F. Serwane, G. Zürn, T. Lompe, T. B. Ottenstein, A. N. Wenz, and S. Jochim, “Deterministic Preparation of a Tunable Few-Fermion System,” *Science* **332**, 336–338 (2011).
- [41] F. Serwane, *Deterministic Preparation of a Tunable Few-Fermion System*, Ph.D. thesis, Ruprecht-Karls-Universität Heidelberg (2011).
- [42] A. M. Kaufman, B. J. Lester, C. M. Reynolds, M. L. Wall, M. Foss-Feig, K. R. A. Hazzard, A. M. Rey, and C. A. Regal, “Two-particle quantum interference in tunnel-coupled optical tweezers,” *Science* **345**, 306–309 (2014).
- [43] A. M. Kaufman, B. J. Lester, M. Foss-Feig, M. L. Wall, A. M. Rey, and C. A. Regal, “Entangling two transportable neutral atoms via local spin exchange,” *Nature* **527**, 208–211 (2015).
- [44] M. O. Brown, S. R. Muleady, W. J. Dworschack, R. J. Lewis-Swan, A. M. Rey, O. Romero-Isart, and C. A. Regal, “Time-of-flight quantum tomography of an atom in an optical tweezer,” *Nat. Phys.* **19**, 569–573 (2023).
- [45] M. R. Lam, N. Peter, T. Groh, W. Alt, C. Robens, D. Meschede, A. Negretti, S. Montangero, T. Calarco, and A. Alberti, “Demonstration of Quantum Brachistochrones between Distant States of an Atom,” *Phys. Rev. X* **11**, 011035 (2021).
- [46] M. D. Hutchings, J. B. Hertzberg, Y. Liu, N. T. Bronn, G. A. Keefe, M. Brink, J. M. Chow, and B. L. T. Plourde, “Tunable Superconducting Qubits with Flux-Independent Coherence,” *Phys. Rev. Appl.* **8**, 044003 (2017).
- [47] U. Hohenester, P. K. Rekdal, A. Borzì, and J. Schmiedmayer, “Optimal quantum control of Bose-Einstein condensates in magnetic microtraps,” *Phys. Rev. A* **75**, 023602 (2007).
- [48] R. Bücker, J. Grond, S. Manz, T. Berrada, T. Betz, C. Koller, U. Hohenester, T. Schumm, A. Perrin, and J. Schmiedmayer, “Twin-atom beams,” *Nat. Phys.* **7**, 608–611 (2011).
- [49] R. Bücker, T. Berrada, S. van Frank, J.-F. Schaff, T. Schumm, J. Schmiedmayer, G. Jäger, J. Grond, and U. Hohenester, “Vibrational state inversion of a Bose-Einstein condensate: Optimal control and state tomography,” *J. Phys. B: At. Mol. Opt. Phys.* **46**, 104012 (2013).
- [50] G. Jäger, D. M. Reich, M. H. Goerz, C. P. Koch, and U. Hohenester, “Optimal quantum control of Bose-Einstein condensates in magnetic microtraps: Comparison of gradient-ascent-pulse-engineering and Krotov optimization schemes,” *Phys. Rev. A* **90**, 033628 (2014).
- [51] S. van Frank, M. Bonneau, J. Schmiedmayer, S. Hild, C. Gross, M. Cheneau, I. Bloch, T. Pichler, A. Negretti, T. Calarco, and S. Montangero, “Optimal control of complex atomic quantum systems,” *Sci. Rep.* **6**, 34187 (2016).
- [52] D. Hocker, J. Yan, and H. Rabitz, “Optimal nonlinear coherent mode transitions in Bose-Einstein condensates utilizing spatiotemporal controls,” *Phys. Rev. A* **93**, 053612 (2016).
- [53] J. J. W. H. Sørensen, M. O. Aramburu,

- T. Heinzl, and J. F. Sherson, “Quantum optimal control in a chopped basis: Applications in control of Bose-Einstein condensates,” *Phys. Rev. A* **98**, 022119 (2018).
- [54] J. Schmidt, D. Hönig, P. Weckesser, F. Thielemann, T. Schaetz, and L. Karpa, “Mass-selective removal of ions from Paul traps using parametric excitation,” *Appl. Phys. B* **126**, 176 (2020).
- [55] N. Dupont, G. Chatelain, L. Gabardos, M. Arnal, J. Billy, B. Peaudecerf, D. Sugny, and D. Guéry-Odelin, “Quantum State Control of a Bose-Einstein Condensate in an Optical Lattice,” *PRX Quantum* **2**, 040303 (2021).
- [56] S. Xu, J. Schmiedmayer, and B. C. Sanders, “Nonlinear quantum gates for a Bose-Einstein condensate,” *Phys. Rev. Res.* **4**, 023071 (2022).
- [57] T. Calarco, U. Dorner, P. S. Julienne, C. J. Williams, and P. Zoller, “Quantum computations with atoms in optical lattices: Marker qubits and molecular interactions,” *Phys. Rev. A* **70**, 012306 (2004).
- [58] U. Dorner, T. Calarco, P. Zoller, A. Browaeys, and P. Grangier, “Quantum logic via optimal control in holographic dipole traps,” *J. Opt. B: Quantum Semiclass. Opt.* **7**, S341 (2005).
- [59] J. D. Sterk, H. Coakley, J. Goldberg, V. Hietala, J. Lechtenberg, H. McGuinness, D. McMurtrey, L. P. Parazzoli, J. Van Der Wall, and D. Stick, “Closed-loop optimization of fast trapped-ion shuttling with sub-quanta excitation,” *npj Quantum Inf.* **8**, 1–6 (2022).
- [60] S. Puri, S. Boutin, and A. Blais, “Engineering the quantum states of light in a Kerr-nonlinear resonator by two-photon driving,” *npj Quantum Inf.* **3**, 1–7 (2017).
- [61] C. A. Weidner and D. Z. Anderson, “Experimental Demonstration of Shaken-Lattice Interferometry,” *Phys. Rev. Lett.* **120**, 263201 (2018).
- [62] C. Flühmann, T. L. Nguyen, M. Marinelli, V. Negnevitsky, K. Mehta, and J. P. Home, “Encoding a qubit in a trapped-ion mechanical oscillator,” *Nature* **566**, 513–517 (2019).
- [63] K. C. McCormick, J. Keller, S. C. Burd, D. J. Wineland, A. C. Wilson, and D. Leibfried, “Quantum-enhanced sensing of a single-ion mechanical oscillator,” *Nature* **572**, 86–90 (2019).
- [64] L. Podhora, L. Lachman, T. Pham, A. Lešundák, O. Číp, L. Slodička, and R. Filip, “Quantum Non-Gaussianity of Multiphonon States of a Single Atom,” *Phys. Rev. Lett.* **129**, 013602 (2022).
- [65] V. G. Matsos, C. H. Valahu, T. Navickas, A. D. Rao, M. J. Millican, X. C. Kolesnikow, M. J. Biercuk, and T. R. Tan, “Robust and Deterministic Preparation of Bosonic Logical States in a Trapped Ion,” *Phys. Rev. Lett.* **133**, 050602 (2024).
- [66] W. Wang, Y. Wu, Y. Ma, W. Cai, L. Hu, X. Mu, Y. Xu, Z.-J. Chen, H. Wang, Y. P. Song, H. Yuan, C.-L. Zou, L.-M. Duan, and L. Sun, “Heisenberg-limited single-mode quantum metrology in a superconducting circuit,” *Nat. Commun.* **10**, 4382 (2019).
- [67] A. Eickbusch, V. Sivak, A. Z. Ding, S. S. Elder, S. R. Jha, J. Venkatraman, B. Royer, S. M. Girvin, R. J. Schoelkopf, and M. H. Devoret, “Fast universal control of an oscillator with weak dispersive coupling to a qubit,” *Nat. Phys.* **18**, 1464–1469 (2022).
- [68] M. Kudra, M. Kervinen, I. Strandberg, S. Ahmed, M. Scigliuzzo, A. Osman, D. P. Lozano, M. O. Tholén, R. Borgani, D. B. Haviland, G. Ferrini, J. Bylander, A. F. Kockum, F. Quijandria, P. Delsing, and S. Gasparinetti, “Robust Preparation of Wigner-Negative States with Optimized SNAP-Displacement Sequences,” *PRX Quantum* **3**, 030301 (2022).
- [69] M. Endo, R. He, T. Sonoyama, K. Takahashi, T. Kashiwazaki, T. Umeki, S. Takasu, K. Hattori, D. Fukuda, K. Fukui, K. Takase, W. Asavanant, P. Marek, R. Filip, and A. Furusawa, “Non-Gaussian quantum state generation by multi-photon subtraction at the telecommunication wavelength,” *Opt. Express* **31**, 12865–12879 (2023).
- [70] S. Konno, W. Asavanant, F. Hanamura, H. Nagayoshi, K. Fukui, A. Sakaguchi, R. Ide, F. China, M. Yabuno, S. Miki, H. Terai, K. Takase, M. Endo, P. Marek, R. Filip, P. van Loock, and A. Furusawa, “Logical states for fault-tolerant quantum computation with propagating light,” *Science* **383**, 289–293 (2024).
- [71] M. Gutierrez Latorre, G. Higgins, A. Paradkar, T. Bauch, and W. Wieczorek, “Superconducting Microsphere Magnetically Levitated in an Anharmonic Potential with Integrated Magnetic Readout,” *Phys. Rev. Appl.* **19**, 054047 (2023).
- [72] J. Hofer, R. Gross, G. Higgins, H. Huebl, O. F. Kieler, R. Kleiner, D. Koelle, P. Schmidt, J. A. Slater, M. Trupke, K. Uhl, T. Weimann, W. Wieczorek, and M. Aspelmeyer, “High- Q Magnetic Levitation and Control of Superconducting Microspheres at Millikelvin Temperatures,” *Phys. Rev. Lett.* **131**, 043603 (2023).
- [73] M. Fuwa, R. Sakagami, and T. Tamegai, “Ferromagnetic levitation and harmonic trapping of a milligram-scale yttrium iron garnet sphere,” *Phys. Rev. A* **108**, 063511 (2023).
- [74] E. Bonvin, L. Devaud, M. Rossi, A. Militaru, L. Dania, D. S. Bykov, M. Teller, T. E. Northup, L. Novotny, and M. Frimmer, “Hybrid Paul-optical trap with large optical access for levitated optomechanics,” *arXiv:2312.10131* (2023).

- [75] F.-G. Deng, B.-C. Ren, and X.-H. Li, “Quantum hyperentanglement and its applications in quantum information processing,” *Sci. Bull.* **62**, 46 (2017).
- [76] M. O. Brown, T. Thiele, C. Kiehl, T.-W. Hsu, and C. A. Regal, “Gray-Molasses Optical-Tweezer Loading: Controlling Collisions for Scaling Atom-Array Assembly,” *Phys. Rev. X* **9**, 011057 (2019).
- [77] A. M. Kaufman and K.-K. Ni, “Quantum science with optical tweezer arrays of ultracold atoms and molecules,” *Nat. Phys.* **17**, 1324–1333 (2021).
- [78] C. Robens, S. Brakhane, W. Alt, D. Meschede, J. Zopes, and A. Alberti, “Fast, High-Precision Optical Polarization Synthesizer for Ultracold-Atom Experiments,” *Phys. Rev. Appl.* **9**, 034016 (2018).
- [79] M. A. Rol, F. Battistel, F. K. Malinowski, C. C. Bultink, B. M. Tarasinski, R. Vollmer, N. Haider, N. Muthusubramanian, A. Bruno, B. M. Terhal, and L. DiCarlo, “Fast, High-Fidelity Conditional-Phase Gate Exploiting Leakage Interference in Weakly Anharmonic Superconducting Qubits,” *Phys. Rev. Lett.* **123**, 120502 (2019).
- [80] M. A. Rol, L. Ciorciaro, F. K. Malinowski, B. M. Tarasinski, R. E. Sagastizabal, C. C. Bultink, Y. Salathe, N. Haandbaek, J. Sedivy, and L. DiCarlo, “Time-domain characterization and correction of on-chip distortion of control pulses in a quantum processor,” *Appl. Phys. Lett.* **116**, 054001 (2020).
- [81] R. Bücker, T. Berrada, S. van Frank, J.-F. Schaff, T. Schumm, J. Schmiedmayer, G. Jäger, J. Grond, and U. Hohenester, “Vibrational state inversion of a Bose–Einstein condensate: Optimal control and state tomography,” *J. Phys. B: At. Mol. Opt. Phys.* **46**, 104012 (2013).
- [82] M. Dykman, ed., *Fluctuating Nonlinear Oscillators: From Nanomechanics to Quantum Superconducting Circuits* (Oxford University Press, Oxford, United Kingdom, 2012).
- [83] D. Leibfried, R. Blatt, C. Monroe, and D. Wineland, “Quantum dynamics of single trapped ions,” *Rev. Mod. Phys.* **75**, 281–324 (2003).
- [84] C. Gonzalez-Ballester, M. Aspelmeyer, L. Novotny, R. Quidant, and O. Romero-Isart, “Levitodynamics: Levitation and control of microscopic objects in vacuum,” *Science* **374**, eabg3027 (2021).
- [85] M. Roda-Llorges, A. Riera-Campeny, D. Candoli, P. T. Grochowski, and O. Romero-Isart, “Macroscopic Quantum Superpositions via Dynamics in a Wide Double-Well Potential,” *Phys. Rev. Lett.* **132**, 023601 (2024).
- [86] A. Lingenfelter, D. Roberts, and A. A. Clerk, “Unconditional Fock state generation using arbitrarily weak photonic nonlinearities,” *Sci. Adv.* **7**, eabj1916 (2021).
- [87] M. Yuan, A. Seif, A. Lingenfelter, D. I. Schuster, A. A. Clerk, and L. Jiang, “Universal Control in Bosonic Systems with Weak Kerr Nonlinearities,” [arXiv:2312.15783](https://arxiv.org/abs/2312.15783) (2023).
- [88] J. Werschnik and E. K. U. Gross, “Quantum optimal control theory,” *J. Phys. B: At. Mol. Opt. Phys.* **40**, R175 (2007).
- [89] N. V. Vitanov, A. A. Rangelov, B. W. Shore, and K. Bergmann, “Stimulated Raman adiabatic passage in physics, chemistry, and beyond,” *Rev. Mod. Phys.* **89**, 015006 (2017).
- [90] D. Guéry-Odelin, A. Ruschhaupt, A. Kiely, E. Torrontegui, S. Martínez-Garaot, and J. G. Muga, “Shortcuts to adiabaticity: Concepts, methods, and applications,” *Rev. Mod. Phys.* **91**, 045001 (2019).
- [91] M. H. Levitt, “Composite pulses,” *Prog. Nucl. Magn. Reson. Spectrosc.* **18**, 61–122 (1986).
- [92] N. Khaneja, T. Reiss, C. Kehlet, T. Schulte-Herbrüggen, and S. J. Glaser, “Optimal control of coupled spin dynamics: Design of NMR pulse sequences by gradient ascent algorithms,” *J. Magn. Reson.* **172**, 296–305 (2005).
- [93] D. M. Reich, M. Ndong, and C. P. Koch, “Monotonically convergent optimization in quantum control using Krotov’s method,” *J. Chem. Phys.* **136**, 104103 (2012).
- [94] M. Goerz, D. Basilewitsch, F. Gago-Encinas, M. G. Krauss, K. P. Horn, D. M. Reich, and C. Koch, “Krotov: A Python implementation of Krotov’s method for quantum optimal control,” *SciPost Phys.* **7**, 080 (2019).
- [95] J. A. Nelder and R. Mead, “A Simplex Method for Function Minimization,” *Comput. J.* **7**, 308–313 (1965).
- [96] D. Goldberg and K. Sastry, *Genetic Algorithms: The Design of Innovation* (Springer, 2007).
- [97] S. Kirkpatrick, C. D. Gelatt, and M. P. Vecchi, “Optimization by simulated annealing,” *Science* **220**, 671–680 (1983).
- [98] L. Giannelli, S. Sgroi, J. Brown, G. S. Paraoanu, M. Paternostro, E. Paladino, and G. Falci, “A tutorial on optimal control and reinforcement learning methods for quantum technologies,” *Phys. Lett. A* **434**, 128054 (2022).
- [99] M. M. Müller, R. S. Said, F. Jelezko, T. Calarco, and S. Montangero, “One decade of quantum optimal control in the chopped random basis,” *Rep. Prog. Phys.* **85**, 076001 (2022).
- [100] C. Leforestier, R. H. Bisseling, C. Cerjan, M. D. Feit, R. Friesner, A. Guldberg, A. Hammerich, G. Jolicard, W. Karrlein, H. D. Meyer, N. Lipkin, O. Roncero, and R. Kosloff, “A comparison of different propagation schemes for the time

- dependent Schrödinger equation,” *J. Comput. Phys.* **94**, 59–80 (1991).
- [101] W.-L. Ma, S. Puri, R. J. Schoelkopf, M. H. Devoret, S. M. Girvin, and L. Jiang, “Quantum control of bosonic modes with superconducting circuits,” *Sci. Bull.* **66**, 1789–1805 (2021).
- [102] S. Rosenblum, P. Reinhold, M. Mirrahimi, L. Jiang, L. Frunzio, and R. J. Schoelkopf, “Fault-tolerant detection of a quantum error,” *Science* **361**, 266–270 (2018).
- [103] L. H. Pedersen, N. M. Møller, and K. Mølmer, “Fidelity of quantum operations,” *Phys. Lett. A* **367**, 47–51 (2007).
- [104] Z. Leghtas, G. Kirchmair, B. Vlastakis, M. H. Devoret, R. J. Schoelkopf, and M. Mirrahimi, “Deterministic protocol for mapping a qubit to coherent state superpositions in a cavity,” *Phys. Rev. A* **87**, 042315 (2013).
- [105] M. Mirrahimi, Z. Leghtas, V. V. Albert, S. Touzard, R. J. Schoelkopf, L. Jiang, and M. H. Devoret, “Dynamically protected cat-qubits: A new paradigm for universal quantum computation,” *New J. Phys.* **16**, 045014 (2014).
- [106] S. Murmann, A. Bergschneider, V. M. Klinkhamer, G. Zürn, T. Lompe, and S. Jochim, “Two Fermions in a Double Well: Exploring a Fundamental Building Block of the Hubbard Model,” *Phys. Rev. Lett.* **114**, 080402 (2015).
- [107] R. Islam, R. Ma, P. M. Preiss, M. Eric Tai, A. Lukin, M. Rispoli, and M. Greiner, “Measuring entanglement entropy in a quantum many-body system,” *Nature* **528**, 77–83 (2015).
- [108] Z. Z. Yan, B. M. Spar, M. L. Prichard, S. Chi, H.-T. Wei, E. Ibarra-García-Padilla, K. R. A. Hazzard, and W. S. Bakr, “Two-Dimensional Programmable Tweezer Arrays of Fermions,” *Phys. Rev. Lett.* **129**, 123201 (2022).
- [109] N. E. Frattini, R. G. Cortiñas, J. Venkatraman, X. Xiao, Q. Su, C. U. Lei, B. J. Chapman, V. R. Joshi, S. M. Girvin, R. J. Schoelkopf, S. Puri, and M. H. Devoret, “Observation of Pairwise Level Degeneracies and the Quantum Regime of the Arrhenius Law in a Double-Well Parametric Oscillator,” *Phys. Rev. X* **14**, 031040 (2024).
- [110] S. Martínez-Garaot, E. Torrontegui, X. Chen, M. Modugno, D. Guéry-Odelin, S.-Y. Tseng, and J. G. Muga, “Vibrational Mode Multiplexing of Ultracold Atoms,” *Phys. Rev. Lett.* **111**, 213001 (2013).
- [111] J. Beugnon, C. Tuchendler, H. Marion, A. Gaëtan, Y. Miroshnychenko, Y. R. P. Sortais, A. M. Lance, M. P. A. Jones, G. Messin, A. Browaeys, and P. Grangier, “Two-dimensional transport and transfer of a single atomic qubit in optical tweezers,” *Nat. Phys.* **3**, 696–699 (2007).
- [112] A. Fuhrmanek, A. M. Lance, C. Tuchendler, P. Grangier, Y. R. P. Sortais, and A. Browaeys, “Imaging a single atom in a time-of-flight experiment,” *New J. Phys.* **12**, 053028 (2010).
- [113] S. Deffner and S. Campbell, “Quantum speed limits: From Heisenberg’s uncertainty principle to optimal quantum control,” *J. Phys. A: Math. Theor.* **50**, 453001 (2017).
- [114] L. Mandelstam and I. Tamm, “The uncertainty relation between energy and time in nonrelativistic quantum mechanics,” *J. Phys. USSR* **9**, 249 (1945).
- [115] N. Margolus and L. B. Levitin, “The maximum speed of dynamical evolution,” *Physica D* **120**, 188–195 (1998).
- [116] J. Anandan and Y. Aharonov, “Geometry of quantum evolution,” *Phys. Rev. Lett.* **65**, 1697–1700 (1990).
- [117] S. Deffner and E. Lutz, “Energy–time uncertainty relation for driven quantum systems,” *J. Phys. A: Math. Theor.* **46**, 335302 (2013).
- [118] X. Chen and J. G. Muga, “Transient energy excitation in shortcuts to adiabaticity for the time-dependent harmonic oscillator,” *Phys. Rev. A* **82**, 053403 (2010).
- [119] G. Ness, M. R. Lam, W. Alt, D. Meschede, Y. Sagi, and A. Alberti, “Observing crossover between quantum speed limits,” *Sci. Adv.* **7**, eabj9119 (2021).
- [120] K. Mølmer, Y. Castin, and J. Dalibard, “Monte Carlo wave-function method in quantum optics,” *J. Opt. Soc. Am. B* **10**, 524–538 (1993).
- [121] J.-F. Mennemann, D. Matthes, R.-M. Weishäupl, and T. Langen, “Optimal control of Bose–Einstein condensates in three dimensions,” *New J. Phys.* **17**, 113027 (2015).
- [122] M. Roda-Llodes, D. Candoli, P. T. Grochowski, A. Riera-Campenya, T. Agrenius, J. J. García-Ripoll, C. Gonzalez-Ballester, and O. Romero-Isart, “Numerical simulation of large-scale nonlinear open quantum mechanics,” *Phys. Rev. Res.* **6**, 013262 (2024).
- [123] A. Riera-Campenya, M. Roda-Llodes, P. T. Grochowski, and O. Romero-Isart, “Wigner Analysis of Particle Dynamics and Decoherence in Wide Nonharmonic Potentials,” *Quantum* **8**, 1393 (2024).
- [124] C. A. Rosiek, M. Rossi, A. Schliesser, and A. S. Sørensen, “Quadrature Squeezing Enhances Wigner Negativity in a Mechanical Duffing Oscillator,” *PRX Quantum* **5**, 030312 (2024).
- [125] All data and simulation codes are available upon reasonable request at [10.5281/zenodo.11160535](https://doi.org/10.5281/zenodo.11160535).

A Single-well two-level unitary implementations

In this section, we present examples of the implementation of selected unitaries within a two-level subspace spanned by either Fock, GKP, or four-legged-cat states. Fig. 4 shows results for a single-well Gaussian potential, while Fig. A1 concerns a cosine one.

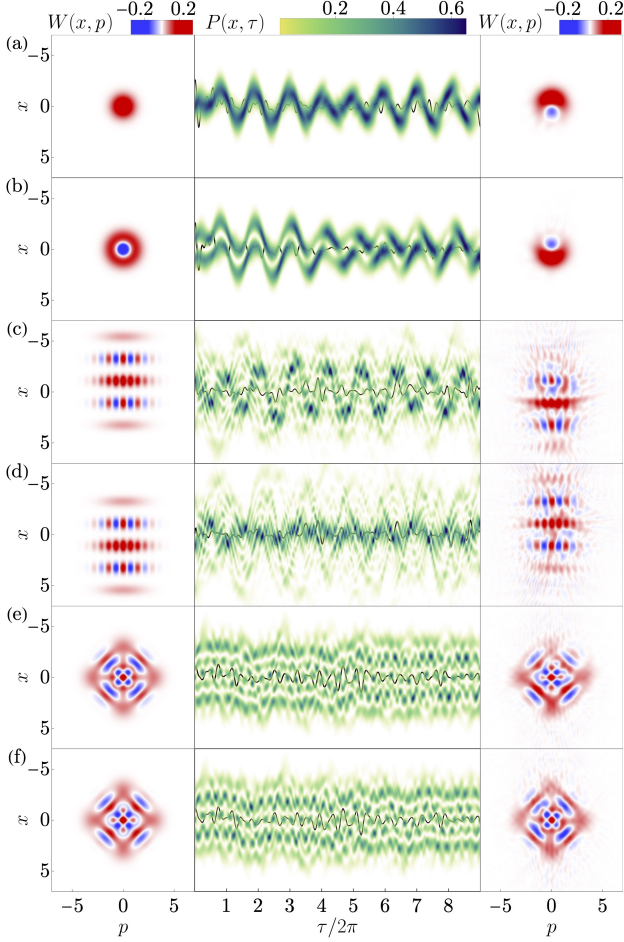


Figure A1: Evolution of selected orthogonal states in a cosine potential characterized by $\eta = 0.2$ and with optimally controlled displacement $u(\tau)$ and intensity $a(\tau)$ that are constrained through the flux control of a flux-tunable transmon with $d = 0.8$. The solid line shows $u(\tau)$ and the protocol lasts $\tau_{\max}/2\pi = 9$. (a-b) Hadamard unitary within a subspace spanned by $|0\rangle$ and $|1\rangle$ Fock states. The fidelity reads $\mathcal{F}_{\hat{U}} \approx 99.99\%$. (c-d) σ_y unitary within a subspace spanned by GKP states, $\psi^\pm = \psi_{\text{GKP}}(x \pm d_3/4)$ with $r = 0.7$, $(d_1, d_2, d_3) = (-\sqrt{6}\pi, 0, \sqrt{6}\pi)$. The fidelity reads $\mathcal{F}_{\hat{U}} \approx 89.5\%$. (e-f) σ_x unitary within a subspace spanned by four-legged-cat states with $\beta = 2$. The fidelity reads $\mathcal{F}_{\hat{U}} \approx 94.0\%$.

B Double-well two-level unitary implementations

In Fig. B1, we present examples of the implementation of selected unitaries within a two-level subspace spanned by Kerr-cat states, $\psi^\pm(x) = [\psi_0(x + s/2) \pm i\psi_0(x - s/2)]/\sqrt{2}$ with $s = 9$ via double-well Gaussian potential with $\eta = 0.25$.

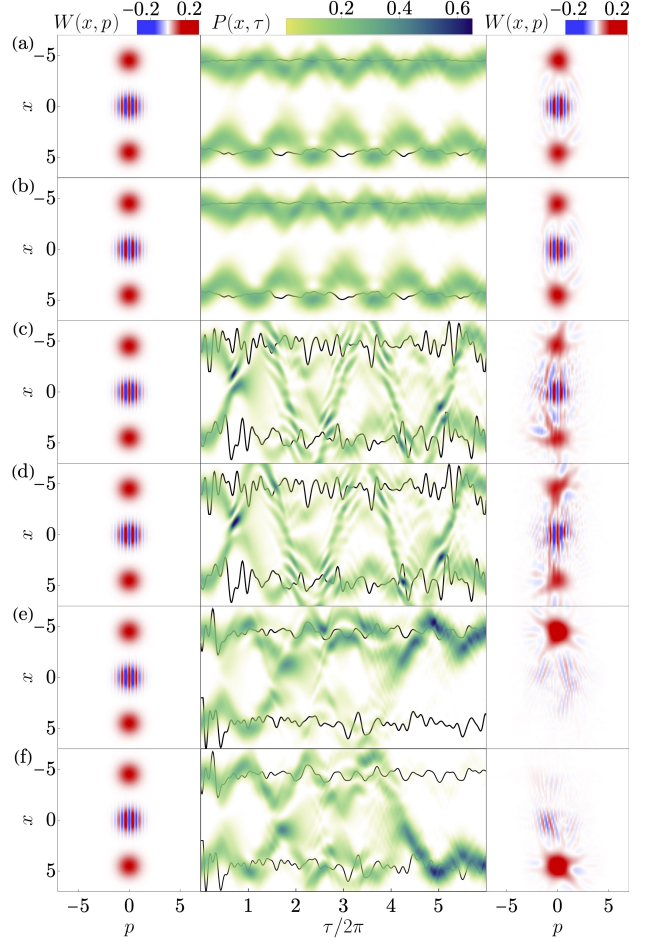


Figure B1: Evolution of selected orthogonal Kerr-cat states in a double-well Gaussian potential with optimally controlled position displacements $u_1(\tau)$ and $u_2(\tau)$. The solid lines show $u_1(\tau)$ and $u_2(\tau)$ and the protocol lasts $\tau_{\max}/2\pi = 6$. (a-b) σ_x unitary. The fidelity reads $\mathcal{F}_{\hat{U}} \approx 99.2\%$. (c-d) σ_x unitary. The fidelity reads $\mathcal{F}_{\hat{U}} \approx 90.9\%$. (e-f) Hadamard unitary. The fidelity reads $\mathcal{F}_{\hat{U}} \approx 95.9\%$.

C Selective stealing protocols

In Fig. C1, we present examples of the implementation of selective stealing protocols via an optimally controlled double-well Gaussian potential with $\eta = 0.25$ and $\tau_{\max}/2\pi = 6$.

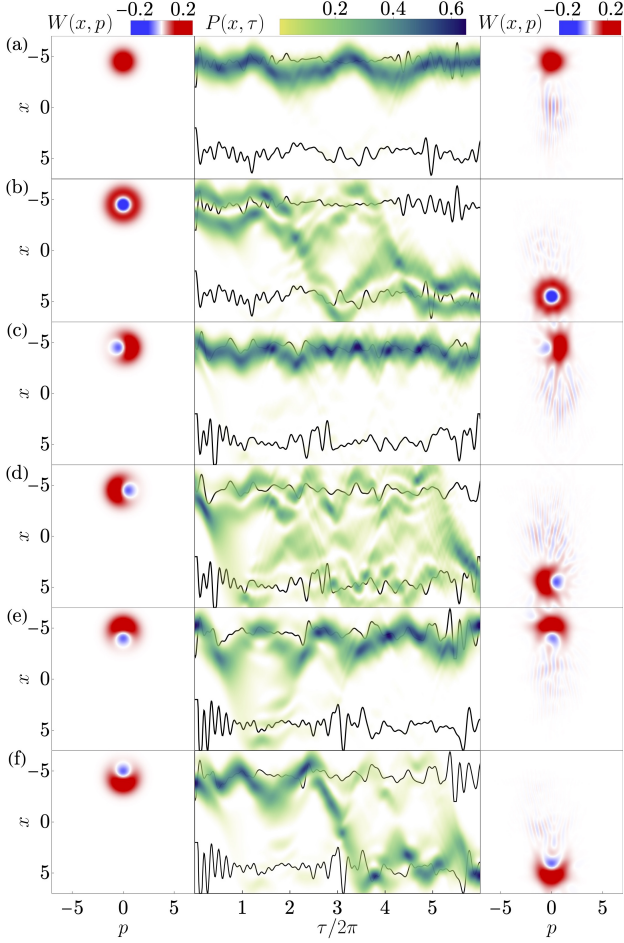


Figure C1: Spatial separation of orthogonal states $\psi^\pm(x + s/2) \rightarrow \psi^\pm(x \mp s/2)$ with $s = 9$ for (a-b) $\psi^+(x) = \psi_0(x)$ and $\psi^-(x) = \psi_1(x)$, (c-d) $\psi^\pm(x) = [\psi_0(x) \pm \psi_1(x)]/\sqrt{2}$, and (e-f) $\psi^\pm(x) = [\psi_0(x) \pm i\psi_1(x)]/\sqrt{2}$. Fidelities read (a-b) $\mathcal{F}_{\hat{U}} \approx 98.9\%$, (c-d) $\mathcal{F}_{\hat{U}} \approx 98.9\%$, and (e-f) $\mathcal{F}_{\hat{U}} \approx 97.4\%$

D Fourier transforms of control functions

In this section, we present Fourier transforms of displacement control functions,

$$\mathfrak{F}_u = \left| \int u(\tau) \exp\left(-i\frac{\tilde{\omega}}{\omega}\tau\right) \right|, \quad (57)$$

for all the presented protocols. Specifically, Figs. D-1, D-3, and D-7 pertain to the figures from the main text, while Figs. D-2, D-4, D-A1, D-B1, D-6, D-C1, and D-10 are associated to the Supplemental Materials.

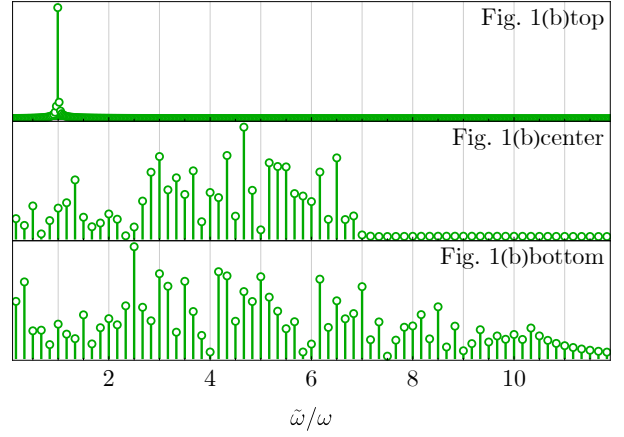


Figure D-1: Fourier transforms of displacement control functions $u(\tau)$ from Fig. 1 in the main text. The vertical axis is in arbitrary units, normalized to the highest frequency contribution.

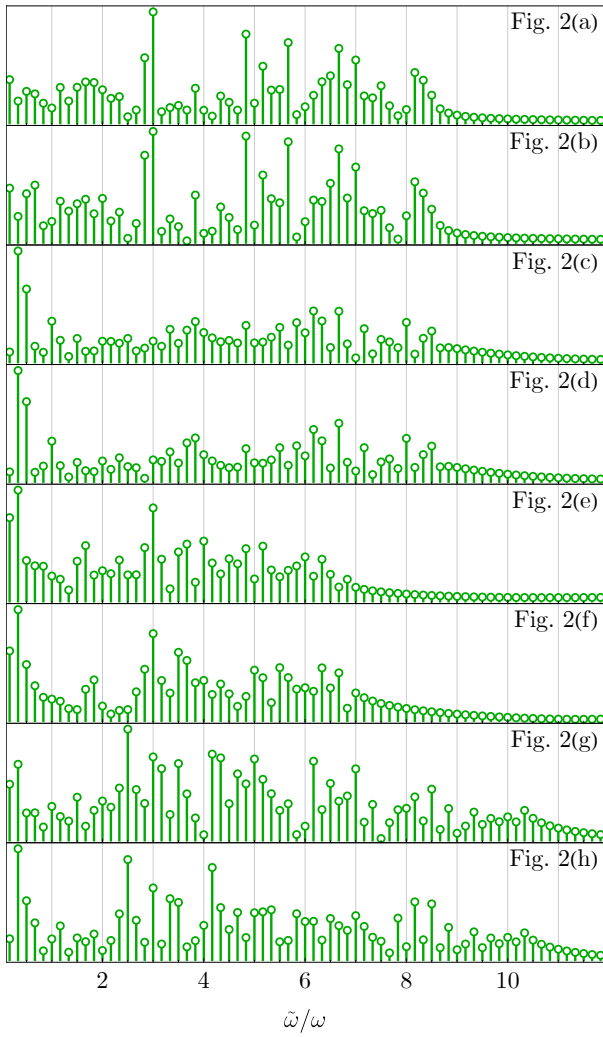


Figure D-2: Fourier transforms of displacement control functions $u(\tau)$ from Fig. 2. The vertical axis is in arbitrary units, normalized to the highest frequency contribution.

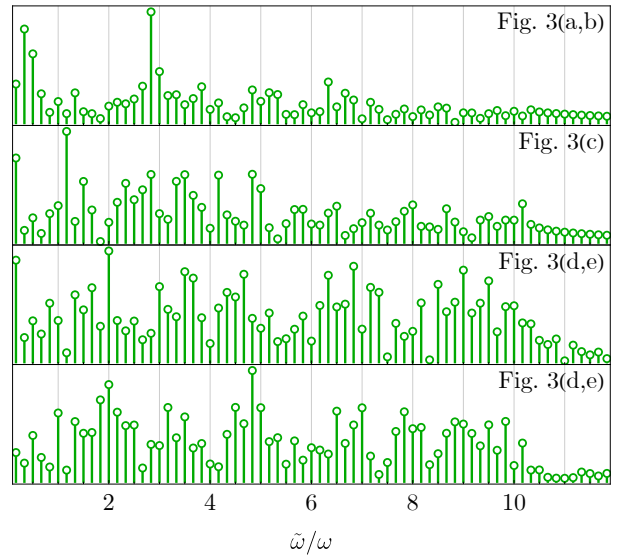


Figure D-3: Fourier transforms of displacement control functions $u(\tau)$ from Fig. 3 in the main text. The vertical axis is in arbitrary units, normalized to the highest frequency contribution.

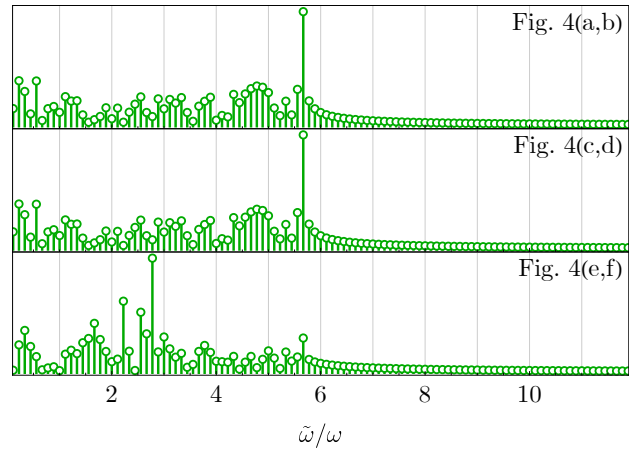


Figure D-4: Fourier transforms of displacement control functions $u(\tau)$ from Fig. 4. The vertical axis is in arbitrary units, normalized to the highest frequency contribution.

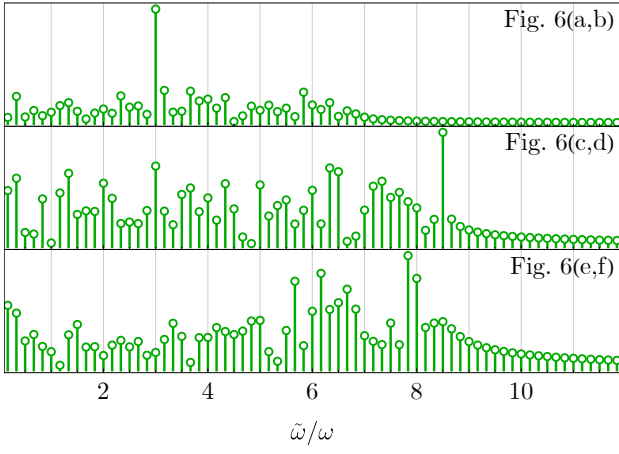


Figure D-6: Fourier transforms of displacement control functions $u(\tau)$ from Fig. 6. The vertical axis is in arbitrary units, normalized to the highest frequency contribution.

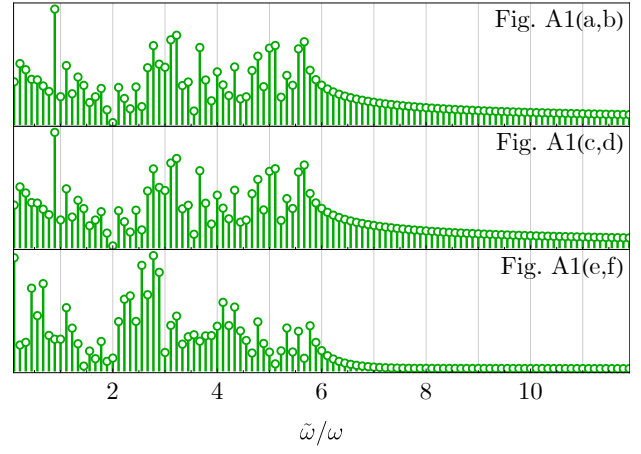


Figure D-A1: Fourier transforms of displacement control functions $u(\tau)$ from Fig. A1. The vertical axis is in arbitrary units, normalized to the highest frequency contribution.

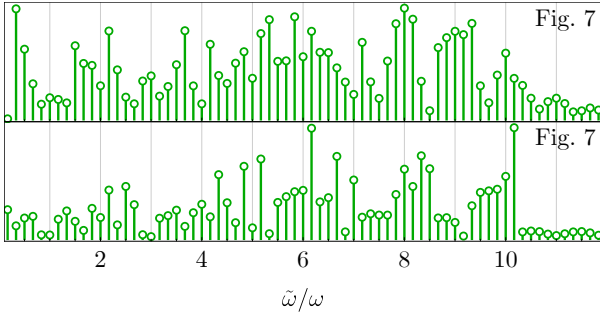


Figure D-7: Fourier transforms of displacement control functions $u(\tau)$ from Fig. 7 in the main text. The vertical axis is in arbitrary units, normalized to the highest frequency contribution.

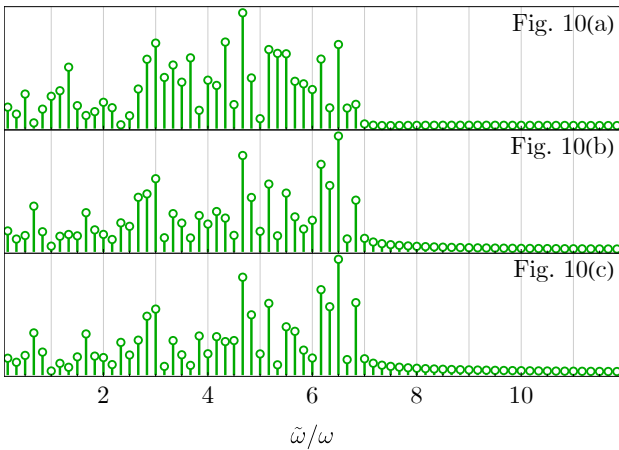


Figure D-10: Fourier transforms of displacement control functions $u(\tau)$ from Fig. 10. The vertical axis is in arbitrary units, normalized to the highest frequency contribution.

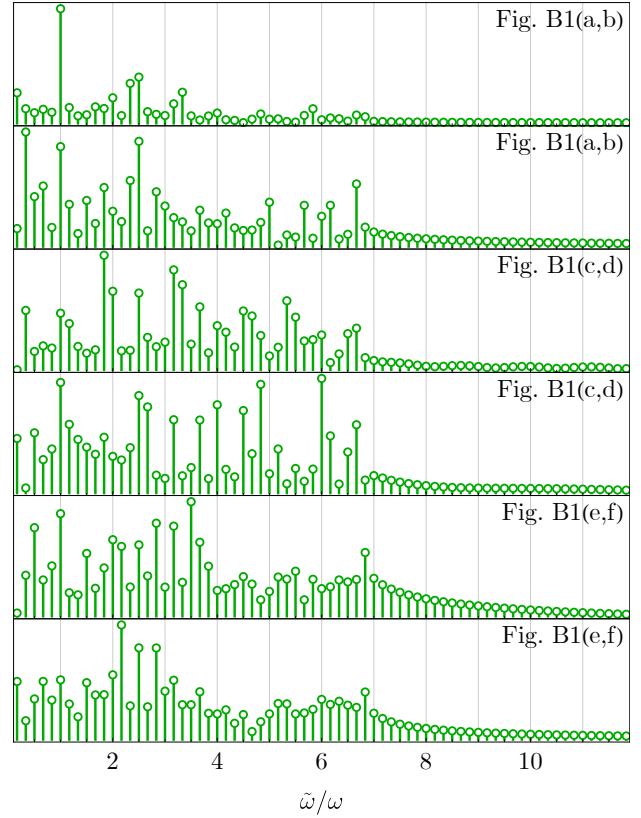


Figure D-B1: Fourier transforms of displacement control functions $u(\tau)$ from Fig. B1. The vertical axis is in arbitrary units, normalized to the highest frequency contribution.

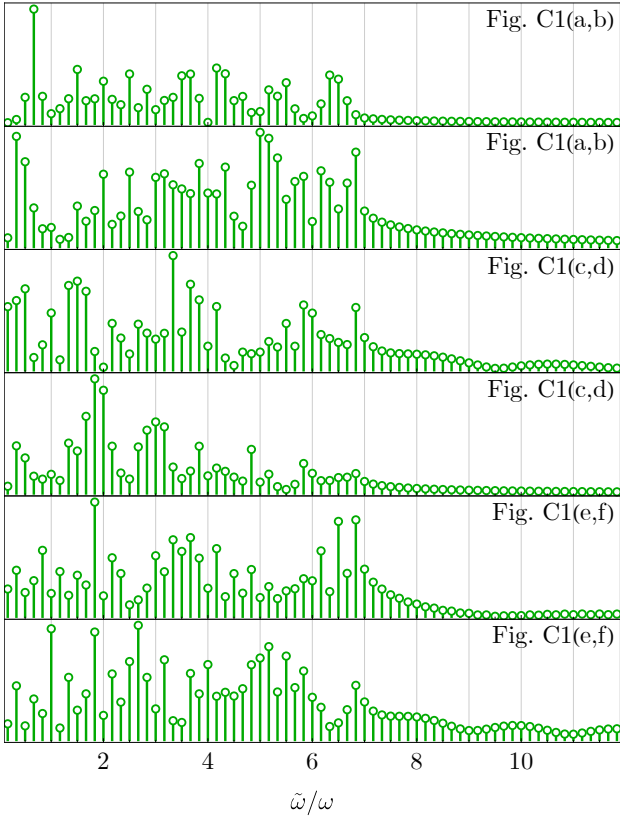


Figure D-C1: Fourier transforms of displacement control functions $u(\tau)$ from Fig. C1. The vertical axis is in arbitrary units, normalized to the highest frequency contribution.

E Depth modulations

Some of the protocols, presented in both the main text and the supplementary materials, utilized additional optimal control of the potential's depth, $a(\tau)$. In Figs. E-3, E-4, and E-6, these control functions are shown.

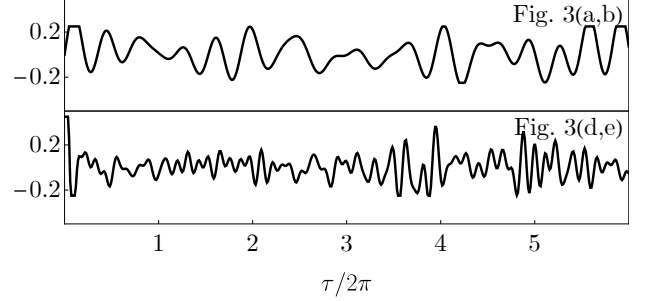


Figure E-3: Depth control functions $a(\tau)$ from Fig. 3.

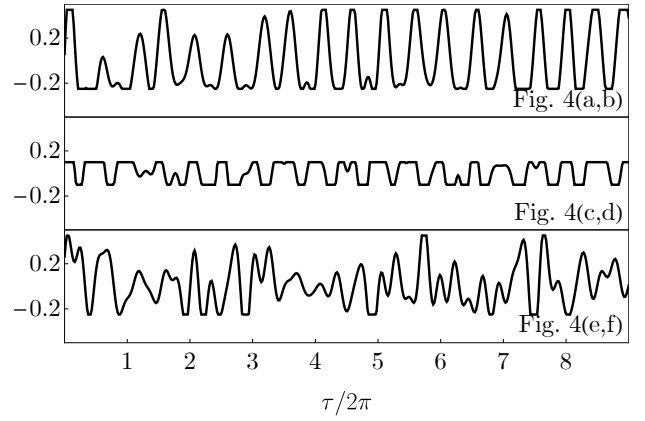


Figure E-4: Depth control functions $a(\tau)$ from Fig. 4.

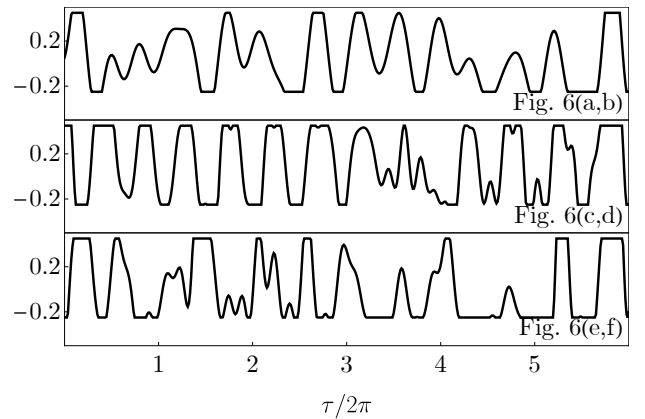


Figure E-6: Depth control functions $a(\tau)$ from Fig. 6.